MODELING THE DYNAMICAL COUPLING OF SOLAR CONVECTION WITH THE RADIATIVE INTERIOR

ALLAN SACHA BRUN[1], MARK S. MIESCH[2], AND JURI TOOMRE[3]

[1] Laboratoire AIM Paris-Saclay, CEA/Irfu Université Paris-Diderot CNRS/INSU, 91191 Gif-sur-Yvette, France
[2] High Altitude Observatory, NCAR, Boulder, CO 80307-3000, USA
[3] JILA & Department of Astrophysical and Planetary Sciences, University of Colorado, Boulder, CO 80309-0440, USA

ABSTRACT

The global dynamics of a rotating star like the Sun involves the coupling of a highly turbulent convective envelope overlying a seemingly benign radiative interior. We use the anelastic spherical harmonic code to develop a new class of three-dimensional models that nonlinearly couple the convective envelope to a deep stable radiative interior. The numerical simulation assumes a realistic solar stratification from $r = 0.07$ up to $0.97R$ (with R the solar radius), thus encompassing part of the nuclear core up through most of the convection zone. We find that a tachocline naturally establishes itself between the differentially rotating convective envelope and the solid body rotation of the interior, with a slow spreading that is here diffusively controlled. The rapid angular momentum redistribution in the convective envelope leads to a fast equator and slow poles, with a conical differential rotation achieved at mid-latitudes, much as has been deduced by helioseismology. The convective motions are able to overshoot downward about $0.04R$ into the radiative interior. However, the convective meridional circulation there is confined to a smaller penetration depth and is directed mostly equatorward at the base of the convection zone. Thermal wind balance is established in the lower convection zone and tachocline but departures are evident in the upper convection zone. Internal gravity waves are excited by the convective overshooting, yielding a complex wave field throughout the radiative interior.

Key words: convection – Sun: interior – Sun: oscillations – Sun: rotation – turbulence – waves

Online-only material: animation, color figures

1. DYNAMICS OF THE SOLAR INTERIOR

As a low-mass star, the Sun possesses a deep convective envelope overlying a relatively quiescent interior where heat transport is achieved by means of radiative diffusion. According to the Schwarzschild criterion (Cox & Giuli 1968), the transition from convective stability to instability occurs near $r = 0.71R$ (with R the solar radius), and is attributed primarily to a large increase in the opacity associated with C, N, and O with increasing radius. The convective envelope, covering the outer 29% by radius, is highly turbulent, involving changes on timescales of minutes to weeks, and it rotates differentially. It also exhibits a variety of magnetic phenomena, most notably the emergence of sunspots and the equatorward migration of activity bands with a characteristic magnetic cycle period of approximately 22 yr. In contrast, the radiative interior evolves on a much longer timescale (of order the Kelvin–Helmholtz time $\sim 10^7$ yr), rotates as a solid body down to at least 0.2–$0.3R$ (Eff-Darwich et al. 2008), and may possess a stable magnetic fossil field. Helioseismology has revealed that the rotation profile throughout the convection zone is similar to that indicated by surface Doppler observations, with little radial variation (Schou et al. 1998; Thompson et al. 2003). The transition to nearly uniform rotation in the radiative interior occurs near the base of the convection zone, across a thin boundary layer known as the solar tachocline (Spiegel & Zahn 1992).

While the dynamics of the convection and radiative zones differ strikingly, they are nevertheless intimately coupled and a comprehensive understanding of solar internal dynamics must take into account their mutual nonlinear interactions. This is a challenging task for numerical models, given the large diversity of physical phenomena that need to be captured at the base of the convection zone, including convective overshoot, anisotropic turbulence, internal wave excitation and propagation, magnetic

field generation and storage, tachocline dynamics and confinement, and hydrodynamic and magnetic instabilities.

1.1. Penetration and Wave Excitation

Turbulent convection in a continuous medium does not simply stop where the stratification shifts from superadiabatic to subadiabatic. At the base of the convection zone, the inertia of downflow plumes carries them into the convectively stable interior where they are buoyantly decelerated over a finite distance. The extent of convective penetration or of overshooting is a function of both the stiffness of the stable zone and the Peclet number $\mathrm{Pe} = vL/\kappa$ (with v and L characteristic velocity and length and κ the thermal diffusivity) associated with the plumes (Zahn 1991; Brummell et al. 2002; Rempel 2004). For large Peclet numbers, the turbulence associated with the braking plumes leads to efficient mixing of the zone, such that its stratification is changed to nearly adiabatic. For low Peclet numbers mixing is inefficient and the stratification remains largely unchanged. Furthermore, the stable radial stratification deflects descending motions horizontally, exciting anisotropic turbulence (Michaud & Zahn 1998). Assessing the degree of such anisotropy and its consequences for the dynamics of the base of the convection zone is a subject of active study (e.g., Miesch 2003; Kim & Leprovost 2007).

Directly connected to convective penetration is the excitation of internal waves by the continuous pummeling of turbulent convective plumes at the top of the radiative zone (Hurlburt et al. 1986; Goldreich & Kumar 1990; Garcia Lopez & Spruit 1991; Zahn et al. 1997; Kiraga et al. 2003; Rogers & Glatzmaier 2005). These waves are internal gravity waves if the rotational influence is negligible, or otherwise mixed inertial-gravity waves (Mathis et al. 2008). Just what wave spectrum is excited by the penetration of convective plumes, how it is modified by the influence of rotation, and how these waves propagate and

transport angular momentum are important issues to assess, for they may contribute to the solid body rotation of the solar radiative interior and the spin-down of the radiative core over secular timescales (Charbonnel & Talon 2005; Rogers & Glatzmaier 2006).

1.2. Rotational History and Transport

Also of general interest is to understand the rotation history of the Sun from its formation through its main-sequence evolution until its final evolutionary phase (Charbonneau & MacGregor 1993; Palacios et al. 2006; Bouvier 2008). How angular momentum is redistributed in the radiative and convection zones as well as how external torques, through interaction with a disk in the T-Tauri phase (Matt & Pudritz 2005; Bessolaz et al. 2008) or a stellar wind (Schatzman 1962; Weber & Davis 1967; Skumanich 1972), influences the Sun's evolution and internal rotation profile is a central issue to resolve (Denissenkov et al. 2010; Spada et al. 2010). We know by studying open clusters at various ages that the distribution of stellar rotation rates shows a larger spread during their early evolutionary phase than later on when they reach the age of the Hyades (Bouvier 2008). The timescale for core-envelope coupling has a direct influence on stellar rotational evolution, with the profile of rotation in the radiative interior (solid body or radial differential rotation) influencing the evolutionary track (Keppens et al. 1995; Irwin et al. 2008; Denissenkov et al. 2010). This coupling timescale is a function of rotation rate and currently its theoretical estimate varies between 1 Myr for fast rotators up to hundreds of Myr for slowly rotating solar-like stars (Pinsonneault 1997; Denissenkov et al. 2010). We thus need to develop models that can improve our knowledge of this coupling and how it occurs.

Just as stellar rotational evolution provides a diagnostic for angular momentum transport between the convection and radiation zones, compositional evolution provides a diagnostic for mass transport. In particular, the surface abundances of light elements such as lithium and beryllium are observed to decrease over the main-sequence lifetime of solar-like stars (Michaud & Charbonneau 1991; Cayrel 1998; Bouvier 2008). This decrease is attributed to transport of chemical species below the convective envelope into the stable radiative interior where light elements are dissociated. Thus, stellar compositional evolution can be used to put constraints on the presence and extent of internal mixing below the convection zone (Brun et al. 1999). Such mixing may be triggered by hydrodynamical (rotational) or MHD instabilities that are associated with the presence of large-scale flows such as differential rotation (Zahn 1992).

1.3. Solar Magnetism

The Sun is a magnetic star, and this greatly complicates its dynamics, particularly with regard to the coupling between the convection and radiation zones. For instance, cold intense downward plumes transport magnetic field via magnetic pumping into the radiative interior (Tobias et al. 2001). This is one of the key ingredients for the current solar interface dynamo paradigm (Parker 1993; Brun et al. 2004; Charbonneau 2010). Effectively, the base of the convection zone is considered as the place to store magnetic field generated in the turbulent convective envelope and to convert it into strong toroidal magnetic field via the radial and latitudinal shear present in the tachocline (Browning et al. 2006; Ghizaru et al. 2010). Internal waves are also modified by the presence of magnetic fields, becoming alveno-gravito-inertial waves (Soward 2007; Campos 2010; Mathis & De Brye

2011). The possible presence of a modest fossil field in the radiative interior may explain the solid body rotation and the thinness of the tachocline (Rüdiger & Kitchatinov 1997, 2007; Gough & McIntyre 1998; Garaud 2002; Brun & Zahn 2006) or be at the origin of magnetic instabilities that might trigger mixing of angular momentum or chemical abundances (Tayler 1973; Spruit 1999). These questions are still debated in the community. The presence of a deep seated magnetic field is also an efficient way of linking angular momentum lost at the solar surface to the inner radiative interior. Here also the observation of other magnetic solar-like stars with various levels of activity, rotation rates, and cycle periods indicates that there is a clear relation between magnetism and rotation: rapidly rotating solar-like stars often exhibit relatively strong magnetic activity (Baliunas et al. 1995; Saar & Brandenburg 1999; Pizzolato et al. 2003). Thus, being able to reconstruct the rotational history and the internal rotation profile of the Sun can improve significantly our understanding of the evolution of solar-like stars and vice versa.

1.4. Incorporating the Many Elements

Until recently most theoretical developments considered each physical process independently from one another and numerical models of the convection and radiation zones and the tachocline were computed in one dimension or two dimensions (see for instance Pinsonneault 1997; Denissenkov et al. 2010; Rüdiger & Kitchatinov 1997; Spada et al. 2010, and reference therein). Thanks to recent advances in supercomputer architectures it is now possible to tackle the coupled problem in three dimensions with an augmented level of realism. Previous attempts to model the coupling between the convective and radiative zones using the three dimensional (3D) anelastic spherical harmonic (ASH) code (Clune et al. 1999) have considered a shallow radiative zone ($r_{bot} \sim 0.6R$) below the convective envelope with various degrees of turbulence and magnetism (Glatzmaier 1985, 1987; Miesch et al. 2000; Browning et al. 2006). A simpler approach was also used where a latitudinal entropy gradient was imposed at the base of a convective envelope to mimic the presence of a tachocline (Miesch et al. 2006, hereinafter MBT06). In this paper, we are setting the stage for a subsequent new series of 3D MHD models of the Sun with the ASH code that seek to address as extensively as possible the questions raised above. We start here with the hydrodynamical reference model assuming a realistic solar-like stratification and describe its properties in detail. We have made the deliberate choice of trading high horizontal resolution (as in Miesch et al. 2008) for an extended vertical domain to explore the radiative–convective zone coupling on dynamical timescales. Over the longer term, we intend to apply this new simulation approach to investigate dynamo action in the convection zone and tachocline as well as its interaction with a primordial field embedded in the radiative interior. Some recent efforts with the ASH code have started to address aspects of these complex problems (Strugarek et al. 2011), and more results are forthcoming.

In Section 2, we explain the formulation of the model and the equations solved by ASH. In Section 3, we describe the nonlinear convective motions that develop in the outer 30% of the model and how they penetrate into the radiative interior. In Section 4, we discuss the profile and amplitude of large-scale flows and thermodynamic variables associated with the convection and their extension into the radiative interior, as well as the meridional and zonal force balances achieved in the model. We then study the coupling between the convective and

radiative zones in more detail in Section 5 and reflect on the significance of our findings in Section 6.

2. MODELING APPROACH

2.1. Anelastic Equations

In this paper, we report 3D numerical experiments designed to investigate the complex hydrodynamics (HD) of the solar convection zone in spherical geometries. We have extended our already well-tested hydrodynamic ASH code (see Clune et al. 1999; Miesch et al. 2000; Brun & Toomre 2002, hereinafter BT02) to include a deep radiative zone. Thus, ASH is now able to solve the full set of 3D HD anelastic equations of motion in a rotating, convective, and radiative spherical shell with high resolution on massively parallel computing architectures. These equations are fully nonlinear in velocity variables, but under the anelastic approximation the thermodynamic variables are linearized with respect to a spherically symmetric and evolving mean state having a density $\bar{\rho}$, pressure $\bar{P}$, temperature $\bar{T}$, and specific entropy $\bar{S}$. Fluctuations about this reference state are denoted by ρ, P, T, and S. The resulting equations are (Glatzmaier 1984; Clune et al. 1999)

$$\boldsymbol{\nabla} \cdot (\bar{\rho} \mathbf{v}) = 0, \tag{1}$$

$$\bar{\rho} \left(\frac{\partial \mathbf{v}}{\partial t} + (\mathbf{v} \cdot \boldsymbol{\nabla}) \mathbf{v} \right) = -\boldsymbol{\nabla} P + \rho \mathbf{g}$$
$$- 2\bar{\rho} \boldsymbol{\Omega_o} \times \mathbf{v} - \boldsymbol{\nabla} \cdot \mathcal{D} - [\boldsymbol{\nabla} \bar{P} - \bar{\rho} \mathbf{g}], \tag{2}$$

$$\bar{\rho} \bar{T} \frac{\partial S}{\partial t} + \bar{\rho} \bar{T} \mathbf{v} \cdot \boldsymbol{\nabla} (\bar{S} + S) = \bar{\rho} \epsilon + \boldsymbol{\nabla} \cdot [\kappa_r \bar{\rho} c_p \boldsymbol{\nabla} (\bar{T} + T)$$
$$+ \kappa \bar{\rho} \bar{T} \boldsymbol{\nabla} S + \kappa_0 \bar{\rho} \bar{T} \boldsymbol{\nabla} \bar{S}] + 2\bar{\rho} \nu [e_{ij} e_{ij} - 1/3(\boldsymbol{\nabla} \cdot \mathbf{v})^2], \tag{3}$$

where $\mathbf{v} = (v_r, v_\theta, v_\phi)$ is the local velocity in spherical coordinates in the frame rotating at constant angular velocity $\boldsymbol{\Omega_o}$, $\mathbf{g}$ is the gravitational acceleration, c_p is the specific heat per unit mass at constant pressure, κ_r is the radiative diffusivity, and $\mathcal{D}$ is the viscous stress tensor. The components of $\mathcal{D}$ are given by

$$\mathcal{D}_{ij} = -2\bar{\rho} \nu [e_{ij} - 1/3(\boldsymbol{\nabla} \cdot \mathbf{v})\delta_{ij}], \tag{4}$$

where e_{ij} is the strain rate tensor, and ν, κ, and κ_0 are effective eddy diffusivities. A volume heating term $\bar{\rho} \epsilon$ is also included in these equations, representing energy generation by nuclear burning. In the deep radiative interior the nuclear reactions are at the origin of the energy released at the surface by the Sun. We have assumed a simple representation of the nuclear reaction rate by setting $\epsilon = \epsilon_0 T^n$, with ϵ_0 a constant determined such that the radially integrated heating term equals the solar luminosity at the base of the convection zone and $n = 9$. The exponent n is larger than what is usually used for p–p chains (i.e., $n = 4$) but much smaller than for the CNO cycle, $n \sim 20$ (Clayton 1968). When integrated over the radius, our choice of heating source term yields a good agreement with that of one-dimensional (1D) standard solar models (Brun et al. 2002) in which p–p chains represent about 98% of the energy release and CNO cycles 2%.

To complete the set of equations, we use the linearized equation of state

$$\frac{\rho}{\bar{\rho}} = \frac{P}{\bar{P}} - \frac{T}{\bar{T}} = \frac{P}{\gamma \bar{P}} - \frac{S}{c_p}, \tag{5}$$
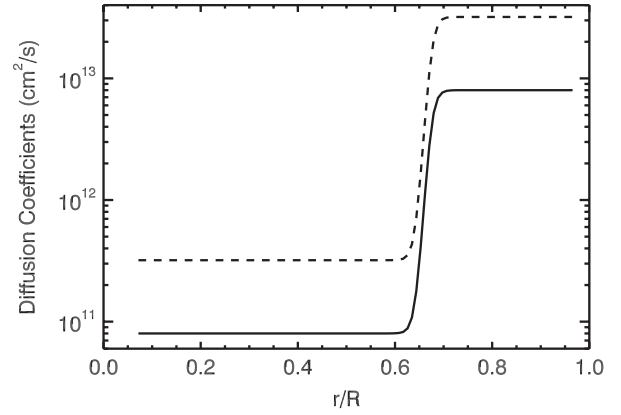
Figure 1. Radial profile of the turbulent kinematic viscosity (solid line) and thermal diffusivity (dashed line) used in the 3D model.

where γ is the adiabatic exponent, and assume the ideal gas law

$$\bar{P} = \mathcal{R} \bar{\rho} \bar{T}, \tag{6}$$

where $\mathcal{R}$ is the gas constant. The reference state is derived from a 1D solar structure model (Brun et al. 2002) and is continuously updated with the spherically symmetric components of the thermodynamic fluctuations as the simulation proceeds. It begins in hydrostatic balance so the bracketed term on the right-hand side (rhs) of Equation (3) initially vanishes. However, as the simulation evolves, turbulent pressure drives the reference state slightly away from hydrostatic balance.

Due to limitations in computing resources, no simulation achievable now or in the near future can hope to directly capture all scales of solar convection from global to molecular dissipation scales. The simulation reported here resolves nonlinear interactions among a large range of scales both in the convective and radiative zones. The nonlinear coupling of the two zones plus the use of a realistic stratification in the radiative interior is what sets this simulation apart. Motions and waves must exist in the Sun on scales smaller than our grid resolution. In this sense, our models should be regarded as large-eddy simulations (LES) with parameterizations to account for subgrid-scale (SGS) motions. Thus, the effective eddy diffusivities ν, κ, and κ_0 represent momentum and heat transport by motions which are not resolved by the simulation. They are allowed to vary with radius but are independent of latitude and longitude, and vary only slightly with time for a given simulation as the reference density evolves. Their amplitudes and radial profiles are varied depending on the resolution and objectives of each simulation. In the simulation reported here, the radial profiles of ν and κ are given by

$$\nu(r) = \nu_{\mathrm{top}} (a + f(r)(1 - a)),$$

with $f(r) = 0.5(\tanh(10^{-10}(r - r_t)/\sigma_t) + 1)$, $\nu_{\mathrm{top}} = 8 \times 10^{12}$ cm^2 s^{-1}, $r_t = 4.7 \times 10^{10}$ cm, $\sigma_t = 0.1$, and $a = 0.01$. For κ, a similar formula is used with $\kappa_{\mathrm{top}} = 3.2 \times 10^{13}$ cm^2 s^{-1} and all of the other parameters kept the same. These tapered profiles are chosen in order to take into account the much smaller SGS transport expected in the convectively stable radiative interior. Their profile is shown in Figure 1. The diffusivity κ_0 is set such as to have the unresolved eddy flux carrying the solar flux outward at the top of the domain (see Figure 4). It drops off exponentially with depth in order to avoid a large inward heat flux in the stable zone (see Miesch et al. 2000). Of course, there is some arbitrariness in choosing the exact shape and amplitude
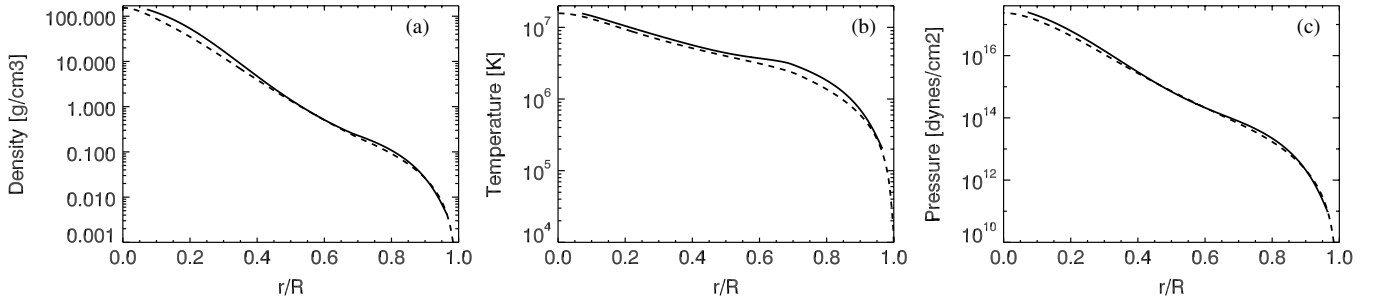
Figure 2. Radial profiles of the (a) density, (b) temperature, and (c) pressure as a function of normalized radius for the 1D standard solar structure model of Brun et al. (2002; dashed lines) and for the reference state $\bar{T}$, $\bar{\rho}$, and $\bar{P}$ used in the 3D ASH convection simulation (solid lines). The reference state for the 3D model is thus chosen to be very close to a 1D seismically calibrated solar model.

of our diffusivity profiles and we do our best to limit their influence on the results reported here.

The velocity and thermodynamic variables are expanded in spherical harmonics $Y_{\ell m}(\theta, \phi)$ for their horizontal structure and in Chebyshev polynomials $T_n(r)$ for their radial structure (see Glatzmaier 1984 and Clune et al. 1999 for more details on the numerical method and anelastic approximation). Two Chebyshev expansion domains are used, meeting below the overshoot region at $r = 4 \times 10^{10}$ cm or $r/R \sim 0.57$.

Given that the convective and radiative zones are nonlinearly and dynamically coupled, internal waves can easily be excited by the pummeling of convective plumes on top of the radiative interior (as was done in two dimensions by Rogers & Glatzmaier 2006). The Brunt-Väisälä frequency N of the model is very close to that deduced from a 1D seismically constrained model (see Figure 8 below). We are thus expecting the propagation of the internal waves to be realistic, aside from the enhanced thermal and viscous diffusion present in the model that translates into an enhanced damping (Zahn et al. 1997). In order to ensure that the mass flux remains divergenceless, we use a toroidal–poloidal decomposition as

$$\bar{\rho}\mathbf{v} = \nabla \times \nabla \times (W\hat{\mathbf{e}}_r) + \nabla \times (Z\hat{\mathbf{e}}_r). \quad (7)$$

This system of hydrodynamic equations requires eight boundary conditions in order to be well posed. Since assessing the angular momentum redistribution in our simulations is one of the main goals of this work, we have opted for the following torque-free velocity conditions.

1. Impenetrable top and bottom: $v_r = 0|_{r=r_{\mathrm{bot}}, r_{\mathrm{top}}}$.
2. Stress free top and bottom:
   $(\partial/\partial r)(v_\theta/r) = (\partial/\partial r)(v_\phi/r) = 0|_{r=r_{\mathrm{bot}}, r_{\mathrm{top}}}$.
3. Constant entropy gradient at top and bottom: $(\partial \bar{S}/\partial r) = 2.2 \times 10^{-3}|_{r=r_{\mathrm{bot}}}$ and $-10^{-7}|_{r=r_{\mathrm{top}}}$.

2.2. Numerical Experiments

Our numerical model is a simplified portrayal of the solar convection and radiative zones: solar values are taken for the heat flux, rotation rate, mass, and radius, and a perfect gas is assumed. The anelastic reference state is based on a 1D standard solar structure model (Brun et al. 2002) as demonstrated in Figures 2 and 3. We initialize the reference state of the 3D model by specifying the entropy gradient $d\bar{S}/dr$ and gravitational acceleration g based on the 1D model. The steep negative entropy gradient near the solar surface is artificially suppressed to avoid the driving of small-scale convective motions that cannot be resolved in this model. We then solve the equation of hydrostatic balance for the reference density $\bar{\rho}$ with a
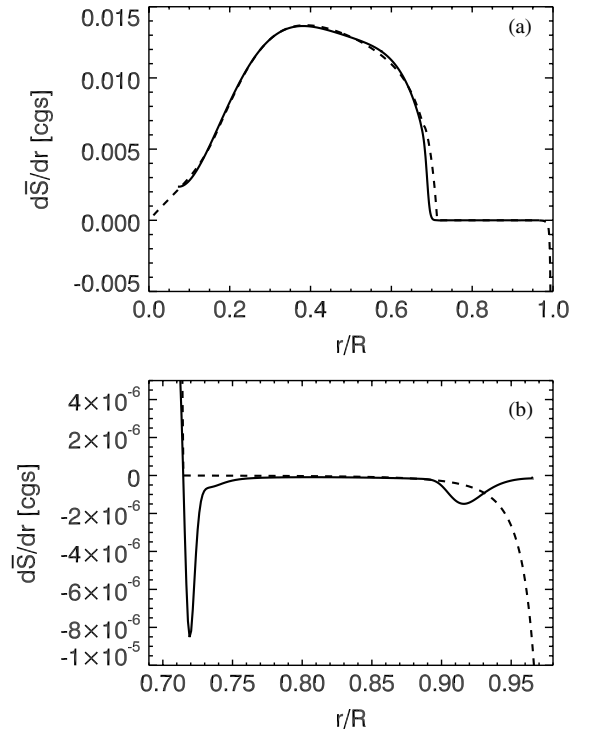
Figure 3. (a) Profile of the mean radial entropy gradient $d\bar{S}/dr$ used as reference state for the 3D simulations (solid lines) compared to the 1D reference solar model of Brun et al. (2002; dashed lines). (b) Zoom in the convective and overshooting region. We clearly see how convective motions modify the entropy gradient in the 3D simulation at the base of the convective domain. The sharp decrease seen in the 1D model beyond $0.95\,R$ has been deliberately attenuated for numerical reasons.

Newton–Raphson method, assuming an ideal gas equation of state and using the density profile of the 1D structure model as an initial guess to initiate the iterative solution. The resulting reference state is close to the solar structure model, with slight departures due to the modified entropy profile in the convection zone and the ideal gas equation of state. Similarly, the radial profile of the radiative diffusivity κ_r is based on the 1D solar structure model, slightly adjusted to accommodate the small changes between the reference state and the structure model.

Thus, the departure of the reference entropy gradient from the solar structure model near the top of the convection zone evident in Figure 3(b) is largely imposed. However, the departure near the base of the convection zone is established by the convection itself, as downflow plumes deposit low entropy material just before entering the stable radiative zone. The initial reference state in this region follows more closely the 1D structure model.
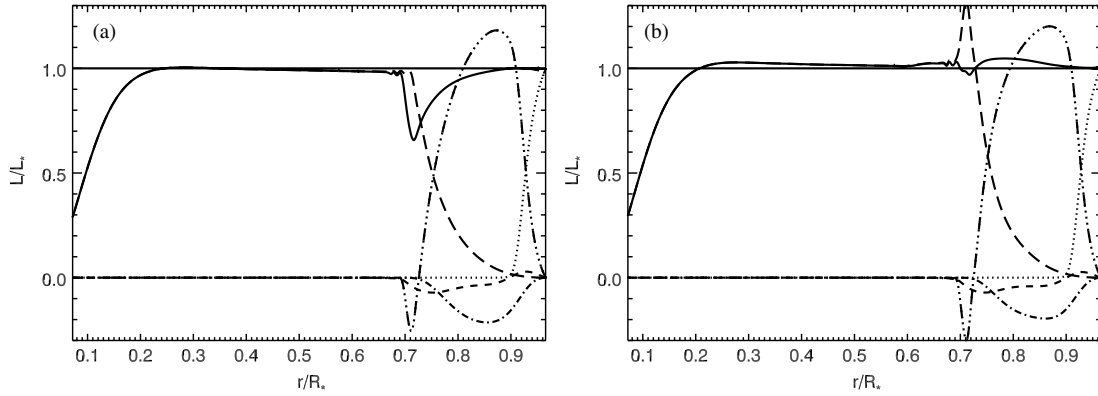
Figure 4. Radial energy flux balance realized in the model (converted into luminosity and normalized to the solar luminosity), (a) before and (b) after adjusting the radiative diffusivity as described in the text. Each figure has been averaged over latitude, longitude, and time, spanning five rotation periods. The good flux balance achieved in panel (b) occurs after having evolved the model for many convective overturning times. Shown from $r = 0.07$ to $0.97R$ are the contributions to the energy flux from radiative diffusion (long dashes), enthalpy (three-dot-dashed), kinetic energy (dash-dot), modeled SGS processes (dots), and viscous diffusion (dashes). The solid line is the sum of all these components. The overshooting region is evident near $0.7R$, characterized by a negative enthalpy flux. In the convection zone the inward kinetic energy flux due to the asymmetry between upflows and downflows is balanced by an outward enthalpy transport that exceeds the solar luminosity.

The computational domain extends from 0.07 to $0.97R$, thereby encompassing 90% of the solar interior by radius. The numerical resolution is $N_r \times N_\theta \times N_\phi = 770 \times 256 \times 512$, with the Chebyshev collocation points providing relatively high radial resolution in the overshooting/tachocline region at the base of the convection zone. Specifically, we have two Chebyshev expansion domains that meet at $r = 0.57R$. This transition point is below the overshoot region but close enough to provide enhanced resolution in this key region of our computational domain. The Gauss–Lobatto collocation scheme provides about 220 mesh points between $r = 0.57R$ and $r = 0.72R$. The average radial spacing grid spacing in this region is approximately 460 km, about 0.7% of the local pressure scale height. The depth of the convection zone r_{bcz}, as defined by the change of sign of the initial mean entropy gradient $d\bar{S}/dr$, is located at $0.71R$ and is slightly modified by the convective motions as the simulation evolves and matures (reaching $0.715R$). At the base of the convection zone proper the resolution is 800 km. The reference density varies across the convective envelope (e.g., $r/R = [0.71, 0.97]$) by about a factor of 30 and by about a factor of 38,000 over the entire computational domain ($r/R = [0.07, 0.97]$).

The energy transport by resolved convective motions will not in general be equivalent to the mixing-length prescriptions assumed in the 1D solar structure model, so the simulation must adjust accordingly. In particular, overshooting convection produces a flux deficit near the base of the convection zone as illustrated in Figure 4(a). Ideally, the system would adjust to a new equilibrium by modifying the background thermal stratification. However, this occurs over a thermal relaxation timescale $E_i/L \sim 10^5$ yr, where E_i is the internal energy of the plasma and L is the luminosity. Since achieving this timescale is impractical, we accelerate the thermal relaxation process by artificially increasing the radiative diffusivity κ_r near the base of the convection zone as described by Miesch et al. (2000). This increase in κ_r is chosen to balance the temporally averaged inward enthalpy flux in the overshoot region (see also Section 3.2 and Figure 6 below). The model subsequently achieves satisfactory flux balance throughout the domain within about 1000 days ($\sim$30–40 convective turnover times), as demonstrated in Figure 4(b). We now proceed to discuss the principal simulation results.

3. DYNAMICS IN THE CONVECTIVE AND RADIATIVE ZONES

Once the convective instability has reached a statistical equilibrium, we evolve the model long enough (several thousand days) to get a mature, well-relaxed dynamical state in order to compute accurate statistics and averages of the main quantities of interest. In this section, we give an overview of the coupled dynamics and flows realized in the convection and radiative zones. We then turn to a more detailed description of the mean flows and the interface region in Sections 4 and 5.

3.1. Convection Patterns

In Figure 5, we show the radial velocity and the temperature fluctuations realized in the model, including layers in the upper and lower convection zones, in the overshoot region, and in the radiative interior. Convective motions are apparent near the top of the domain as a network of narrow downflow lanes surrounding broader upflows. These convective flows are highly time dependent, with convective cells continuously emerging, merging with one another or splitting into two or more distinct structures. Associated with the downflow lanes (upflows) are cool (warm) structures that, given our choice of Prandtl number (1/4), are smoother and broader than the velocity structures. Deeper down, the network of downflow lanes becomes less apparent, with individual convective plumes becoming more isolated as only the strongest downflows pierce through the whole convective envelope. The amplitude of the convective velocity drops significantly (from $200\,\mathrm{m\,s^{-1}}$ down to a $0.1\,\mathrm{m\,s^{-1}}$) within the overshoot region at $r/R = 0.69$ where plumes are buoyantly decelerated. Deeper in the radiative zone, the radial velocity amplitude decreases sharply, reaching a few mm s^{-1} by $r = 0.65R$ and continuing to decrease thereafter. By contrast, the amplitude of the temperature variations is only weakly decreasing with depth, remaining of the order of a few K for the five depths shown.

We note that the strongest downflow plumes in the bulk of the convection zone are also cool (Figures 5(c) and (d)), but typically are surrounded by a sheath of upflow that is warm. As the descending plumes slow down just prior to entering the stable stratification, their fluctuating temperature can reverse sign to become positive as evident at a number of sites, likely due to diffusive heating by their surrounding sheath
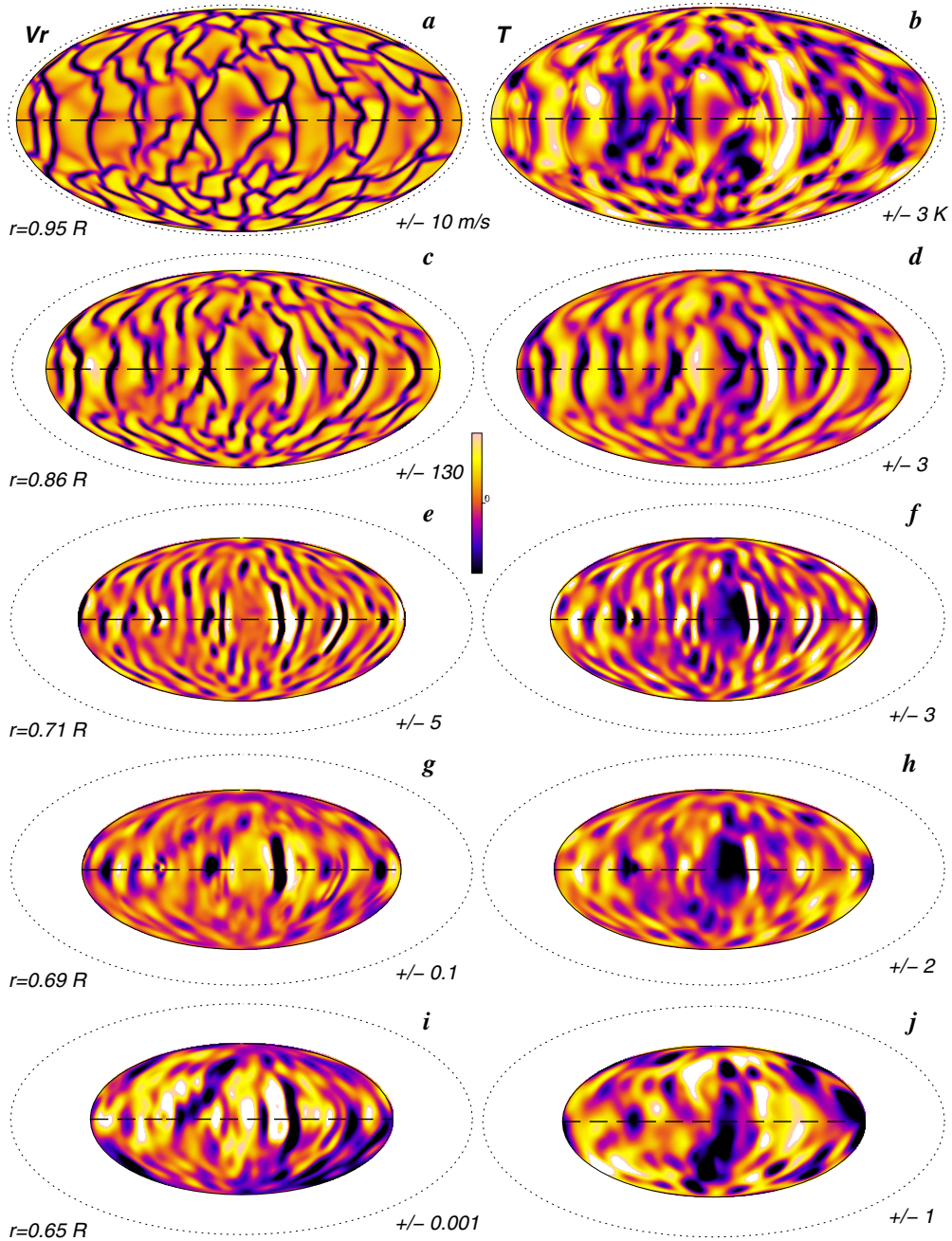
Figure 5. Scaled Mollweide views of the radial velocity (left) and temperature fluctuations (from which we subtracted the $m = 0$ axisymmetric component; right): snapshots, at various radii within the model as indicated. The dotted ellipse corresponds to the solar surface, the dashed line to the equator. Dark tones denote negative (inward) velocities and temperature fluctuations.

(A color version of this figure is available in the online journal.)

(Figures 5(e) and (f)). With increasing depth the downflow sites can become sites of feeble upflow near the top of the radiative interior (Figure 5(i)), largely because the downflows are deflected sideways and viscous diffusion induces an upflow into such divergence sites. These plumes also excite relaxation oscillations in the form of internal gravity waves, some of which contribute to the more rapidly evolving patterns seen at the lowest depths in a single snapshot.

3.2. Penetration of Convective Motions

In the overshoot region the correlation between radial velocity and temperature fluctuations reverses due to the sharp transition from superadiabatic to subadiabatic stratification. As downflow plumes pass through this transition, they are buoyantly decelerated, forming an overshoot region as discussed in Section 1.1. Since the amount of overshooting depends on the stratification (i.e., stiffness or subadiabaticity) of the radiative interior, our use of a realistic solar stratification is a significant achievement, unprecedented in previous global 3D simulations of penetrative convection.

The Peclet number (Pe) of the individual plumes is of essential importance in determining the properties of overshooting convection (see Zahn 1991; Brummell et al. 2002; Browning et al. 2004; Rempel 2004; Rogers et al. 2006; Chan 2010). Small values of Pe give rise to convective overshoot, in the
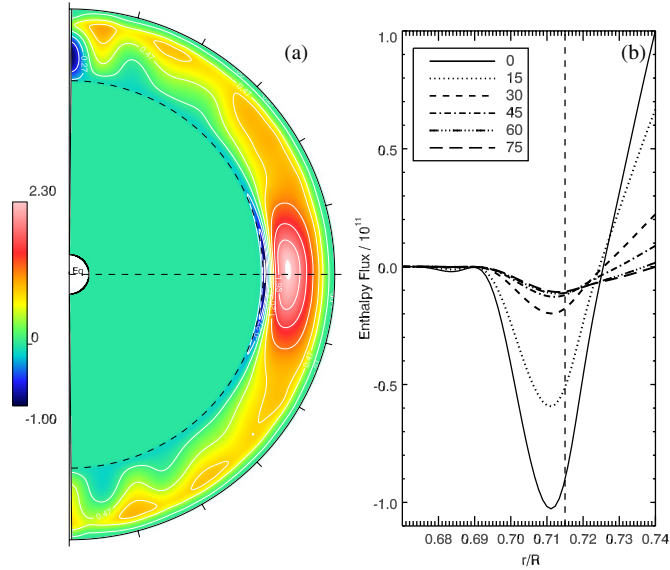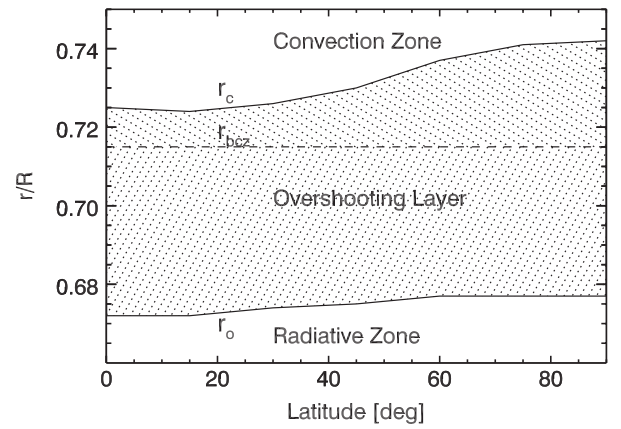
Figure 6. Azimuthal and temporal averages of the radial enthalpy flux in the model (normalized by a factor of 10^{11}). Shown are (a) color contours in the full domain and (b) radial cuts at specified latitudes zooming into the overshoot region. In both panels the base of the convection zone $r_{\rm bcz}$ is indicated by a dashed line (circular in panel (a), vertical in panel (b)), as defined by the change of sign of the mean entropy gradient, $d\bar{S}/dr$. Clearly evident is the negative peak near the base of the convection zone, signifying buoyant braking of convective plumes.

(A color version of this figure is available in the online journal.)

Figure 7. Latitudinal variation of r_c (the radius at which the enthalpy flux becomes negative; top solid line) and r_o (the radius at which the radial enthalpy flux becomes negligible; bottom solid line). The hashed zone is one measure of the extent of the overshoot region, or in other words, the region of mixing. The mean value of r_c is $0.733R$, somewhat higher than the value of $0.715R$ deduced from the change of sign of the mean entropy gradient, so we distinguish these two zones (e.g., below and above $r_{\rm bcz}$) by using a different angle for the dotted lines. We further note the deeper extent of the low-latitude regions, signifying a prolate shape of the bottom of the convective zone and the nearly spherical profile of the bottom of the mixing region, r_o.

sense that the stratification remains significantly subadiabatic. By contrast, high values of Pe promote efficient mixing such that the stratification immediately below the convection zone is nearly adiabatic ($d\bar{S}/dr \sim 0$) and the base of the convection zone can potentially spread downward with time. Following Zahn (1991), we refer to this as convective *penetration* (see also Section 1.1). It is clear that the Peclet number in this mildly turbulent simulation is much less than that of the Sun. Therefore, we may expect to see overshoot as opposed to penetration. This is indeed the case; as demonstrated in Figure 3(b), the stratification below the convection zone is substantially subadiabatic and does not spread with time. Yet the width of the overshoot region may well be overestimated, for it scales as the square root of the filling factor of downflow plumes, which is likely larger in this relatively laminar model than it is in the Sun (Zahn 1991; Rempel 2004).

In Figure 6, we display a temporal and azimuthal average of the radial enthalpy flux along with radial cuts near the base of the convection zone for indicated latitudes. The enthalpy flux peaks in the convective envelope, being predominantly positive at all latitudes. Its maximum is reached at low latitudes, and its profile becomes more skewed toward the top of the domain at high latitudes. Near the base of the convection zone the enthalpy flux becomes negative, as discussed in Section 2.2, again peaking in amplitude and extent at low latitudes. The prominent low-latitude enthalpy flux in the convection zone and overshoot region is a consequence of the relatively laminar convective motions; equatorial modes are linearly preferred in rotating spherical shells near the critical Rayleigh number for the onset of convection. At higher Rayleigh numbers, we expect the radial heat flux to become more homogeneous, filling in higher latitudes (e.g., Miesch et al. 2000). Also, the warm poles and the low Prandtl number further inhibit the enthalpy flux in downward high-latitude plumes.

The negative enthalpy flux at the base of the convection zone is one measure of the extent of the overshoot region. Thus, the latitudinal variation evident in Figure 6(b) reflects a latitudinal variation in the amount of convective overshoot. Following Browning et al. (2004), we quantify this by defining r_c as the radius where the enthalpy flux F_e first changes sign (the node closest to the convection zone) and r_o as the radius below which the amplitude of F_e drops to 0.1% of its most negative value. There is some arbitrariness in the definition of r_o but we find that the results are insensitive to this. The latitudinal variation of r_c and r_o is shown in Figure 7.

Figure 7 indicates that the base of the convection zone as defined by r_c is deeper near the equator than the poles, with a difference of roughly $0.02R$. The mean value of r_c is $0.733R$, which is somewhat higher than the base of the convection zone as defined by the change in sign of the mean entropy gradient, which gives $r_{\rm bcz} = 0.715R$ (see Figure 3). The bottom of the overshoot region r_o is also deeper at the equator but the variation is less, approximately $0.005R$. This implies that the depth of the overshoot region is also larger at the equator. It is certainly of some interest that r_c is greater than $r_{\rm bcz}$ where the mean entropy gradient changes sign. This property arises from some of the downflow plumes having a change in the sign of their fluctuating temperature (from relatively cool to warm) that precedes their arrival at $r_{\rm bcz}$. We attribute this to diffusive heating from their surrounding warm sheaths of upflow serving to warm them and initiating buoyancy braking, accompanied also by a change in the sign of the enthalpy flux (Figure 6(b)) at a depth that varies with latitude.

This result differs from what was found with convective cores in more massive A-type stars by Browning et al. (2004). They find that convection is more extended near the poles and they attribute this to the influence of the Coriolis force, which inhibits the radial motion of overshooting plumes and lanes at low latitudes. Here the more intense convection near the equator and the comparatively slower rotation rate (higher Rossby number) both act to enhance the low-latitude overshoot relative to higher latitudes. Furthermore, the "flywheel" action of persistent, rotationally aligned convective columns (banana

cells) can enhance downward overshoot more efficiently than upward overshoot, as from a convective core (Brummell et al. 2002). This occurs because the preferred columnar (banana) modes tend to hug the tangent cylinder, a cylindrical surface aligned with the rotation axis and tangent to the base of the convection zone. In short, convective overshoot (and, by extension, convective penetration at higher Pe) tends to shift the tangent cylinder closer to the rotation axis.

The overshoot region defined by r_c and r_o may also be regarded as the region below the convection zone proper where turbulent mixing is still appreciable. Thus, r_o marks the location above which the convective envelope can be considered as well mixed. The latitudinal variations shown in Figure 7 then imply that the base of the convection zone as defined by r_c is prolate, whereas the base of the mixing region as defined by r_o is nearly spherical, the latter located near $r = 0.675R$. If we instead define the base of the convection zone in terms of where the radial entropy gradient changes sign, $r_{\rm bcz}$, then this too is nearly spherical, showing no significant latitudinal variation. For reference the diffusivity profiles (cf. Figure 1) possess a transition radius at $0.675R$, which lies near the bottom of the overshoot region.

It is interesting to compare these results with inferences made from helioseismology. Helioseismic structure inversions are sensitive to where the stratification changes from nearly adiabatic to substantially subadiabatic (e.g., Christensen-Dalsgaard et al. 2011). In our case, since we see no significant penetration as opposed to overshooting, this would correspond to $r_{\rm bcz}$. The lack of any significant latitudinal variation in the base of the convection zone inferred from helioseismic structure inversions is thus consistent with the nearly spherical structure of $r_{\rm bcz}$ and also r_o (e.g., Basu & Antia 2001). However, if angular momentum transport is dynamically linked to convective enthalpy transport, then there may be some connection between the prolate structure of r_c and the prolate structure of the tachocline inferred from helioseismic rotational inversions (Charbonneau et al. 1999; Basu & Antia 2001).

The difference between r_c and r_o is one of many ways to define the extent of the overshoot region, yielding an average value of $0.058R$. Here we use an alternative, more robust measure by defining the overshoot region as the region between the base of the convection zone as traced by a change in sign of the mean radial entropy gradient, $r_{\rm bcz}$, and the bottom of the mixed layer, r_o. This yields $d_{ov} = r_{\rm bcz} - r_o \sim 0.04R = 28$ Mm, or about 0.43 local pressure scale height ($H_p \sim 65$ Mm at these depths). This value is rather large when compared to theoretical estimates (Zahn 1991) but in agreement with the value quoted by Rogers & Glatzmaier (2006) in their two-dimensional simulations of penetrative solar convection in the equatorial plane. The discrepancy with theoretical estimates may be due to the relatively large filling factor of our convective downflow plumes, which tends to increase the extent of overshooting, as noted above. The filling factor for turbulent, 3D plumes is likely to be smaller than that in 2D simulations or mildly turbulent 3D simulations such as that reported here. More turbulent convective simulations have indeed yielded smaller overshooting depths (Brummell et al. 2002; Browning et al. 2004).
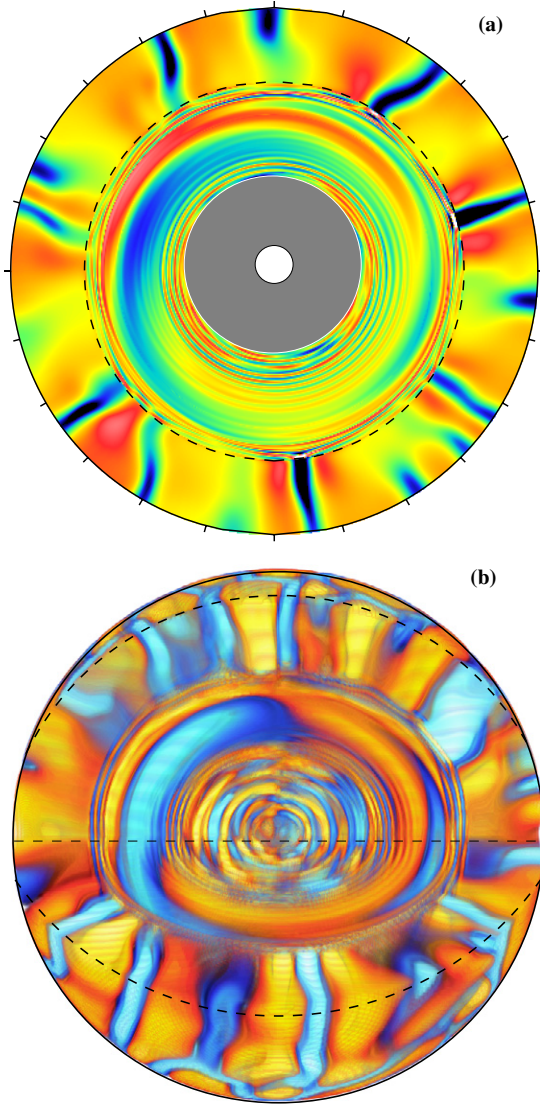
3.3. Gravity Waves

The pummeling of convective plumes on the top of the radiative zone generates a rich field of internal gravity waves (e.g., Hurlburt et al. 1986, 1994; Zahn et al. 1997; Kiraga et al. 2003; Rogers & Glatzmaier 2005). Turning to a snapshot of normalized radial velocities in both an equatorial slice and a cut-away of our full domain, as in Figures 8(a) and (b), the gravity waves appear as the curved, largely horizontal striations evident below the base of the convection zone. In studying a temporal sequence of such equatorial slices, as provided in the accompanying auxiliary movie, they clearly show phase fronts moving consistently radially outward over the upper reaches of the radiative interior, which is a signature of gravity wave packets whose group velocity is inward and phase velocity is outward. In our display here, we have normalized the velocities of the waves by their rms value at each radial level to make them visible, for the actual wave amplitudes decrease by many orders of magnitude in the deep interior, being likely damped by our enhanced thermal diffusion. That rapid decrease in wave amplitudes in proceeding inward in the radiative zone is shown in Figure 8(c), where we display the rms velocity components over the full computational domain. Once the radial velocity amplitudes get below the precision of our numerical scheme, suggesting spurious signals, we proceed to gray out the innermost portion of the domain in Figure 8(a). The prominence of the horizontal velocity components in Figure 8(c) in the radiative interior is consistent with gravity waves possessing much smaller radial wavelengths than horizontal ones. Close scrutiny shows that high radial wavenumber waves permeate the radiative interior, from the base of the convection zone down to at least $0.4R$, beyond which the velocity amplitudes become extremely small. Thus any packet of gravity waves traveling downward in our model dissipates long before it reaches the inner boundary. It is also interesting that Figure 8(a) shows the presence of a large-scale spiral wave structure (with azimuthal order $m = 1$) in the radiative interior that both waxes and wanes in strength and whose phase propagates gradually outward. This suggests that low-degree global gravity wave resonances can potentially be excited in such a system, but are likely dependent on the diffusivity profiles used in our modeling. The conditions for existence of such low-degree resonant modes in our model need to be more accurately determined and we expect to do so in the near future.
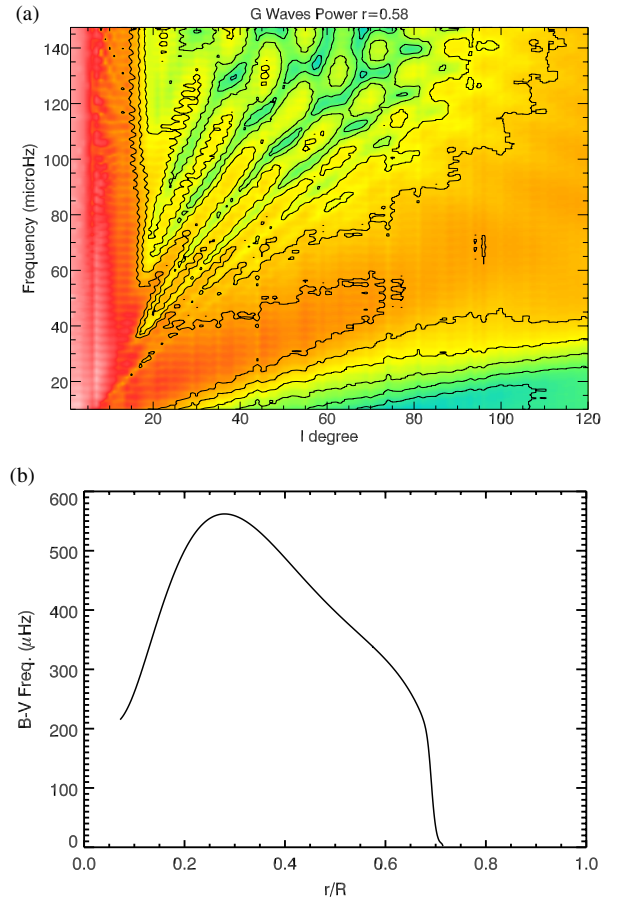
Since the overshooting of the convection extends to about $r_o \simeq 0.672R$ near the equator (Figure 7), whereas the stable mean stratification in terms of $d\bar{S}/dr$ is already established at $0.715R$ (Figure 3(b)), the downward-directed plumes can be quite effective in exciting internal gravity waves in this intermediate region. Figures 8(a) and (b) show that there are many sites of downflow plumes, with these shifting their positions and strengths gradually over periods of hours and days, serving as fairly random and localized gravity wave generators. With the Brunt-Väisälä frequency (being the high-frequency cutoff for locally propagating gravity waves) becoming of the order of 200μHz (or a period of 1.39 hr) already at, say, $0.68R$ as shown in Figure 9(b), one can expect to see a wide range of internal gravity waves excited with frequencies lower than that. Indeed, the power spectrum in Figure 9(a) of frequency versus harmonic degree ℓ of the radial velocities measured on the spherical surface $r = 0.58R$ shows a ridge structure that may be expected for gravity waves, with such features likely to become more evident in longer analysis intervals (here examining 115 days of evolution). The fineness of time sampling used to generate Figure 9(a) is not adequate to capture the full wave spectrum; the abscissa extends to about 140μ Hz whereas the peak Brunt-Väisälä frequency is 550μ Hz (Figure 9(b)). We reserve detailed analyses of the wave spectra and transport for a forthcoming paper.

(a)

(b)

G Waves Power r=0.58

(a)

(b)

Figure 9. (a) Power spectra of the radial velocity in the radiative interior at $r = 0.58R$. The ordinate is the temporal frequency in μHz and the abscissa is the spherical harmonic degree ℓ, with power summed over azimuthal order m. The ridge structure is indicative of gravity waves. (b) Radial profile of the Brunt-Väisälä frequency in the 3D model.

(A color version of this figure is available in the online journal.)

(c)

Figure 8. (a) Equatorial slice ($\theta = \pi/2$, all ϕ) and (b) 3D rendering at same instant, showing the normalized radial velocity v_r/v_{rms} where v_{rms} is the rms radial velocity at each radius, with dark tones denoting downflows. In panel (b) a quadrant has been removed in order to visualize the structure within the meridional and equatorial planes. The presence in the radiative interior of internal waves of various amplitudes and scales is apparent in both panels. In panel (a) the deepest portion of the interior is grayed out because the amplitude drops so low that the signal there may be spurious. (c) Radial profile of three components of the rms velocity. We note the fast drop in amplitude of v_{rms}^r, and the zone below $r < 0.3R$ where the signal becomes extremely weak and reaches numerical precision.

(An animation and a color version of this figure are available in the online journal.)

The role of internal waves is important to assess since they transport angular momentum and can thereby affect the internal rotation profile on both short and long timescales (e.g., Zahn et al. 1997; Miesch 2003; Charbonnel & Talon 2005; Rogers & Glatzmaier 2006; Mathis et al. 2008). The work reported here is a notable step forward in modeling the coupled dynamics of penetrative convection and internal waves in the Sun, being the first 3D, global, solar convection simulation that spans 90% of the solar interior by radius with a fairly sensible solar stratification and rotation rate. In particular, we use a realistic entropy profile in the radiative zone (Figure 3), which allows a wide spectrum of waves to be excited with frequencies comparable to the g modes that are believed to exist in the Sun (Garcia et al. 2007). However, we readily acknowledge that this simulation has a number of shortcomings. We have chosen to focus on global 3D dynamics and the self-consistent, nonlinear coupling between a convective and radiative zone within the context of the Sun. Thus, we must necessarily sacrifice fine spatial resolution which in turn implies enhanced dissipation. Although we have achieved relatively low diffusion in the stable zone through the use of a tapering function as described in Section 2.1, the simulation is still much more diffusive than the solar interior and this likely has adverse implications for wave propagation and transport. Thus, relative to the solar interior, the waves travel shorter distances and are likely less
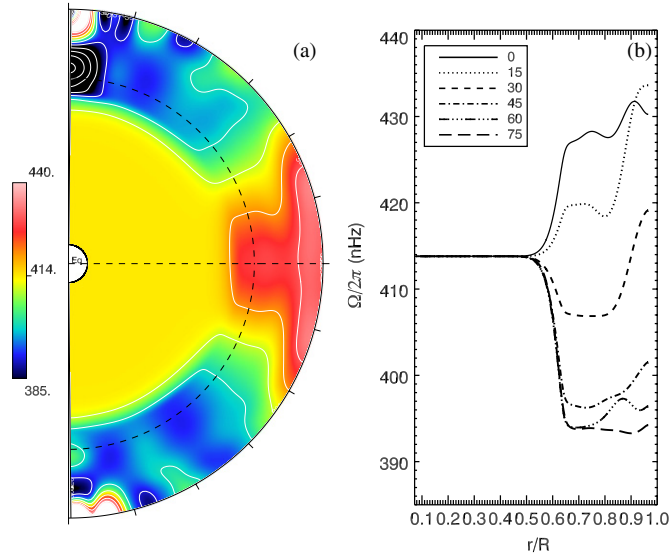
Figure 10. Differential rotation profiles of (a) angular velocity Ω contours averaged over longitude and time. (b) Radial cuts at selected latitudes (after averaging the northern and southern hemispheres) serve to highlight the substantial shear layer at the base of the convection zone, effectively the tachocline, which is naturally realized in the model.

(A color version of this figure is available in the online journal.)

efficient at exciting global resonant g modes. This is seen in the extremely low amplitude of the wave signal near the bottom of the simulation domain (e.g., Figure 8(c)). Even so, the waves in our simulation are well resolved and we believe that their propagation near the top of the radiative zone is reliably captured. Furthermore, since the waves are dissipated well before they reach the inner boundary, we believe that the wave spectrum is likely not sensitive to the inner boundary conditions. We should emphasize that few efforts have been made to minimize thermal damping of the waves or to impose special conditions for their reflection at the inner boundary. We expect to do so in the near future and to compare the wave properties and excitation to theoretical predictions (e.g., Goldreich & Kumar 1990; Garcia Lopez & Spruit 1991; Mathis et al. 2008; Belkacem et al. 2009).

4. GLOBAL MEAN FLOWS AND THERMAL PROPERTIES

Our simulation has been initialized by assuming a uniform state of rotation at all depths and latitudes. The development of the convection instability above $r \sim 0.7R$ and its maturation over several rotation periods leads to the establishment of both large-scale axisymmetric differential rotation and of meridional circulation (Glatzmaier & Gilman 1982; Thompson et al. 2003; Miesch 2005; Brun & Rempel 2008; Miesch & Toomre 2009). We here discuss their properties, focusing in particular on the base of the convection zone.

4.1. Rotation Profile and the Tachocline

In Figure 10, we display the internal rotation profile obtained in our model after about 2000 days of evolution, using both color contours and radial cuts at indicated latitudes. The temporal average spans 10 solar rotation periods. We clearly see that a large-scale differential rotation has been established in the convective envelope. The differential rotation has a fast equator, slow poles, and possesses a conical shape at mid-latitude, much as deduced by helioseismology (Thompson et al. 2003). The
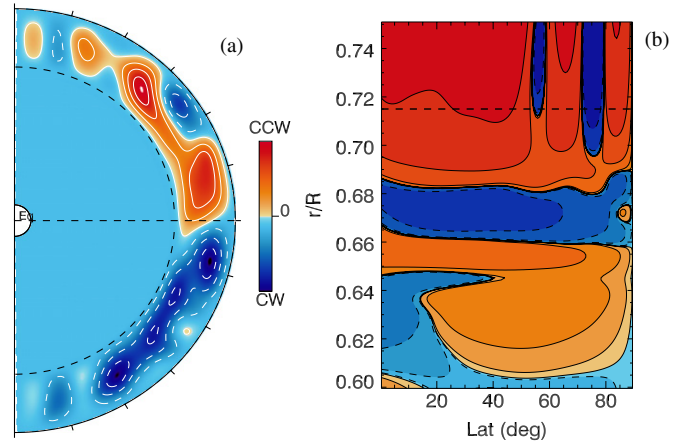
Figure 11. Meridional circulation averaged over longitude and time (over 10 rotation periods), shown by means of the mass flux stream function Ψ. (a) Meridional cut over the whole domain, and (b) zoom-in on the northern hemisphere near the tachocline. Clockwise and counterclockwise circulations are indicated by blue and red tones respectively (and solid/dotted contours).

(A color version of this figure is available in the online journal.)

latitudinal contrast from the equator to about $60°$ at the surface of the model is about 45 nHz, somewhat less than the solar value of about 90 Hz. As the simulation evolves, a sharp transition from the differentially rotating convective envelope to the uniform rotation of the radiative interior develops. This tachocline naturally appears in our simulation and at the time shown in Figure 10 is about $0.10R$ in thickness. This is somewhat larger than indicated by helioseismic rotational inversions which suggest that the width of the tachocline is no more than $0.05R$ (Corbard et al. 1999; Thompson et al. 2003). Even so, our global model of the Sun thus establishes and maintains a very realistic internal rotation profile in good agreement with helioseismic inversions both in the convection zone and at its base. This is a very promising result and a first step toward a full nonlinear dynamical model of the Sun.

4.2. Meridional Flows

In Figure 11(a), we display the meridional circulation realized in the model as contours of the meridional stream function Ψ, defined as in Miesch et al. (2000):

$$r \sin \theta \langle \bar{\rho} v_r \rangle = -\frac{1}{r} \frac{\partial \Psi}{\partial \theta} \text{ and } r \sin \theta \langle \bar{\rho} v_\theta \rangle = \frac{\partial \Psi}{\partial r}.$$

This flow is mostly poleward in the upper convection zone and equatorward in the lower convection zone with one primary cell per hemisphere extending from the equator to more than $60°$ in latitude. We also note the existence of small countercells at mid-latitudes and of a somewhat more complex multi-cell structure near the poles. The flow amplitude is about 20 m s^{-1} near the top of our domain. In Figure 11(b), we display a zoomed-in view of Ψ near the tachocline, spanning the northern hemisphere. This allow us to assess the penetration depth of the meridional circulation, which has been a subject of debate in the community (Gilman & Miesch 2004; Garaud & Brummell 2008). We note that it is mostly confined above $r \sim 0.68R$. This corresponds to a penetration of $0.03R$ if we consider the base of the convection as being defined by the change of sign of the entropy gradient (r_{bcz}). The direction of the flow is equatorward at the base of the convection zone (as in Miesch et al. 2000), with multiple countercells deeper in the radiative interior. These
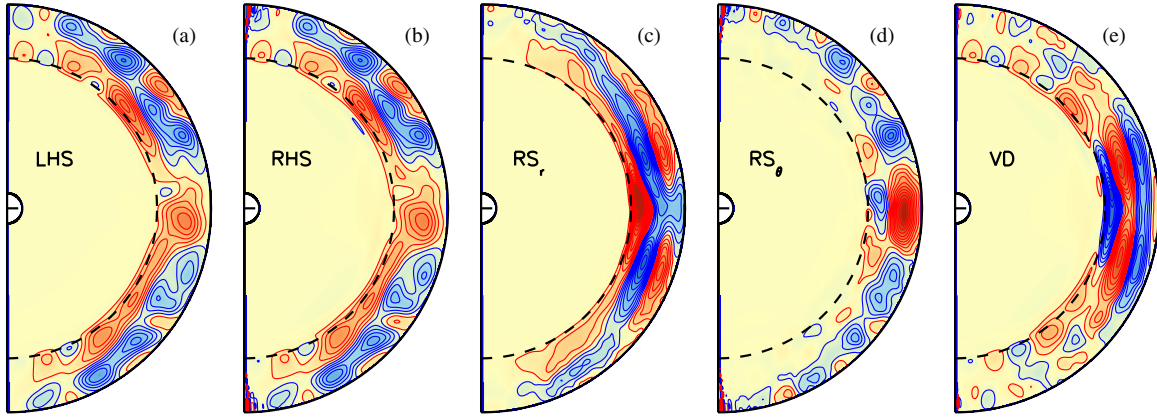
Figure 12. Angular momentum balance, emphasizing gyroscopic pumping of the meridional circulation. Shown are (a) the left-hand side (excluding the term with the time derivative) and (b) the right-hand side of Equation (8). These represent in turn the angular momentum transport by the meridional circulation $\langle \bar{\rho} \mathbf{v}_m \rangle \cdot \boldsymbol{\nabla} \mathcal{L}$ and the net torque $\mathcal{T}$. The net torque includes contributions from (c) the radial and (d) the latitudinal angular momentum transport by the convective Reynolds stress as well as (e) the viscous diffusion. All quantities are averaged over a period of 100 days and share a common color table with a saturation range of $\pm 9.10 \times 10^6$ erg cm^{-3}. Red and blue indicate positive and negative values, respectively. Thus, in frames (b) and (c) red indicates an acceleration of the local rotation rate while blue indicates a deceleration. These are approximately balanced by the advection term in (a), implying statistically steady mean flows.
(A color version of this figure is available in the online journal.)

deeper meridional cells are less intense by several orders of magnitude and are linked to the spread of the tachocline, as discussed in Section 5.1.

4.3. Maintenance of Mean Flows

The differential rotation and meridional circulation profiles in our simulation are established and maintained through the transport of momentum and energy by convective motions that are influenced by the rotation, stratification, and spherical shell geometry. In particular, averaging the zonal (ϕ) component of the momentum equation over longitude and time yields an evolution equation for the specific angular momentum $\mathcal{L}$, which we express here as

$$\bar{\rho}\frac{\partial \mathcal{L}}{\partial t} + \langle \bar{\rho}\mathbf{v}_m \rangle \cdot \boldsymbol{\nabla}\mathcal{L} = -\boldsymbol{\nabla} \cdot (\mathcal{F}_r \hat{\mathbf{e}}_r + \mathcal{F}_\theta \hat{\mathbf{e}}_\theta) \equiv \mathcal{T}, \qquad (8)$$

where

$$\mathcal{L} = \lambda^2 \Omega = \lambda(\langle v_\phi \rangle + \lambda \Omega_0), \qquad (9)$$

and $\lambda = r \sin\theta$ is the moment arm. The radial and latitudinal angular momentum fluxes $\mathcal{F}_r$ and $\mathcal{F}_\theta$ include contributions from the convective Reynolds stress and viscous diffusion (Elliott et al. 2000; Brun & Toomre 2002):

$$\mathcal{F}_r = \bar{\rho}r\sin\theta \left[\underbrace{-\nu r \frac{\partial}{\partial r}\left(\frac{\hat{v}_\phi}{r}\right)}_{\mathcal{F}_{r,V}} + \underbrace{\widehat{v_r' v_\phi'}}_{\mathcal{F}_{r,R}} \right] \qquad (10)$$

$$\mathcal{F}_\theta = \bar{\rho}r\sin\theta \left[\underbrace{-\nu\frac{\sin\theta}{r} \frac{\partial}{\partial \theta}\left(\frac{\hat{v}_\phi}{\sin\theta}\right)}_{\mathcal{F}_{\theta,V}} + \underbrace{\widehat{v_\theta' v_\phi'}}_{\mathcal{F}_{\theta,R}} \right].$$

Our stress-free boundary conditions imply that the volume-integrated transport terms vanish so the total angular momentum $\int \bar{\rho}\mathcal{L}\,dV$, is conserved. We find that this is indeed satisfied in our simulation to within 10^{-7}.

The transport of angular momentum by the mean meridional circulation $\bar{\rho}\mathbf{v}_m$ may also be incorporated into the flux terms

$\mathcal{F}_r$ and $\mathcal{F}_\theta$, but here we write it separately on the left-hand side (lhs) of Equation (8) in order to illustrate more clearly how mean flows are established. Thus, we can regard the Reynolds stress and the viscous diffusion as a net torque $\mathcal{T}$, which, in a statistically steady state ($\partial\mathcal{L}/\partial t = 0$), must balance the advection of angular momentum by the meridional circulation (Equation (8)). Although the angular velocity profile Ω is approximately conical at mid-latitudes (Figure 10(a)), the specific angular momentum $\mathcal{L}$ is more cylindrical, increasing with distance from the rotation axis. Thus, Equation (8) implies that a net prograde torque $\mathcal{T} > 0$ will induce a steady meridional flow away from the rotation axis while a retrograde torque $\mathcal{T} < 0$ will induce a flow toward the rotation axis. This balance is achieved in part through Coriolis-induced acceleration of the meridional circulation by the differential rotation but it is a distinct phenomenon, since it reflects the zonal force balance and the conservation of angular as well as linear momentum. Following McIntyre (1998, 2007), we refer to it as gyroscopic pumping (see also Haynes et al. 1991).

Figure 12 illustrates the dynamical balance expressed in Equation (8) as manifested in our simulation, averaged over approximately 10 rotation periods. The close correspondence between Figures 12(a) and (b) demonstrates that the mean flows in the convection zone have reached an equilibrated state that is approximately stationary in a statistical sense. Thus, there is an approximate balance between the advection of angular momentum by the meridional circulation (Figure 12(a)) and the net torque (Figure 12(b)), which includes contributions from the convective Reynolds stress (Figures 12(c) and (d)) and the viscous diffusion (Figures 12(e)).

The differential rotation (Figure 10(a)) is maintained primarily by the convective Reynolds stress, which transports angular momentum toward the equator, producing a flux convergence in the upper convection zone that accelerates lower latitudes relative to higher latitudes (Figure 12(d)). This equatorward transport is partially offset by a radially inward transport of angular momentum by the Reynolds stress (Figure 12(c)) and viscous diffusion (Figure 12(e)) but it is strong enough to exert a positive net torque (Figure 12(b)). This net torque in turn induces a radially outward flow by means of gyroscopic pumping

that crosses $\mathcal{L}$ contours and then turns poleward near the surface (Figures 11(a) and 12(a)).

Above the equator but at latitudes still low enough to be outside the tangent cylinder, the radial Reynolds stress is negative at mid-depth, decelerating the mid-convection zone and positive at both boundaries, thus accelerating the upper convection zone and the overshoot region (Figure 11(c)). The outward transport arises through the shear-induced tilting of columnar convection cells (banana cells; see, e.g., Busse 2002) while the inward transport arises from the buoyant deceleration of helical downflow plumes (Miesch et al. 2000). Inside the tangent cylinder, banana cells are suppressed and the rotation vector is nearly vertical, promoting transport by helical plumes. The resulting inward angular momentum transport accelerates the rotation rate in the lower convection zone and overshoot region (Figures 12(b) and (c)), promoting an equatorward meridional flow by means of gyroscopic pumping (Figures 11(a) and 12(a)).

4.4. Entropy and Temperature Fluctuations

The thermal structure of the convection zone and its coupling to the tachocline play a key role in establishing the non-cylindrical rotation profile in the solar convection zone (Kitchatinov & Rüdiger 1995; von Rekowski & Rudiger 1998; Durney 1999; BT02; Rempel 2005; MBT06; Balbus et al. 2009; Brun et al. 2010, hereinafter BAC10). This is directly linked to the so-called Taylor–Proudman constraint on rotating flows, e.g., fast rotation tends to make flows invariant along the rotation axis (cylindrical), and this constraint may be broken in the Sun. We have just seen that our model exhibits a conical differential rotation, with a fast equator and slow poles in good agreement with the helioseismic inversions. This is an important result since this feature has emerged naturally from our simulation. No forcing was imposed at the base of the convection zone to realize such a realistic profile contrary to Rempel (2005) or MBT06. We expect baroclinic effects via the so-called thermal wind equation (Pedlosky 1987; Zahn 1992; Durney 1999; BT02; Balbus et al. 2009; BAC10; see the next section) to play a major role. Thus, we now consider the thermal gradients realized in our model and their implications with regard to maintenance of the mean flows.

Figure 13 shows the fluctuations of entropy and temperature with respect to the mean (spherically averaged) temperature $\bar{T}$ of the model. The poleward entropy and temperature gradient in the deep convection zone is in good agreement with previous results, and confirms the role of latitudinal entropy variations in maintaining solar-like (conical) rotation profiles. The mean temperature variation in the upper convection zone is approximately 5–7 K, with a minimum at mid-latitudes. Stronger thermal gradients occur near the base of the convection zone where the latitudinal temperature variation is monotonic, increasing by 9–10 K from equator to pole. These temperature and entropy gradients are comparable to those found in MBT06 but here they are established self-consistently by the internal dynamics, rather than promoted by means of a lower boundary condition. In MBT06, imposed variations at the base of the convection zone exceeding about 13 K yield nearly disk-like rotation profiles. Thus, it is remarkable that the natural dynamics of the coupled convection zone and radiative zone system in this simulation naturally establishes thermal gradients conducive to a solar-like rotation profile, with a strong radial gradient in the tachocline and conical isosurfaces in the convection zone. We now address how these thermal gradients influence mean flows.
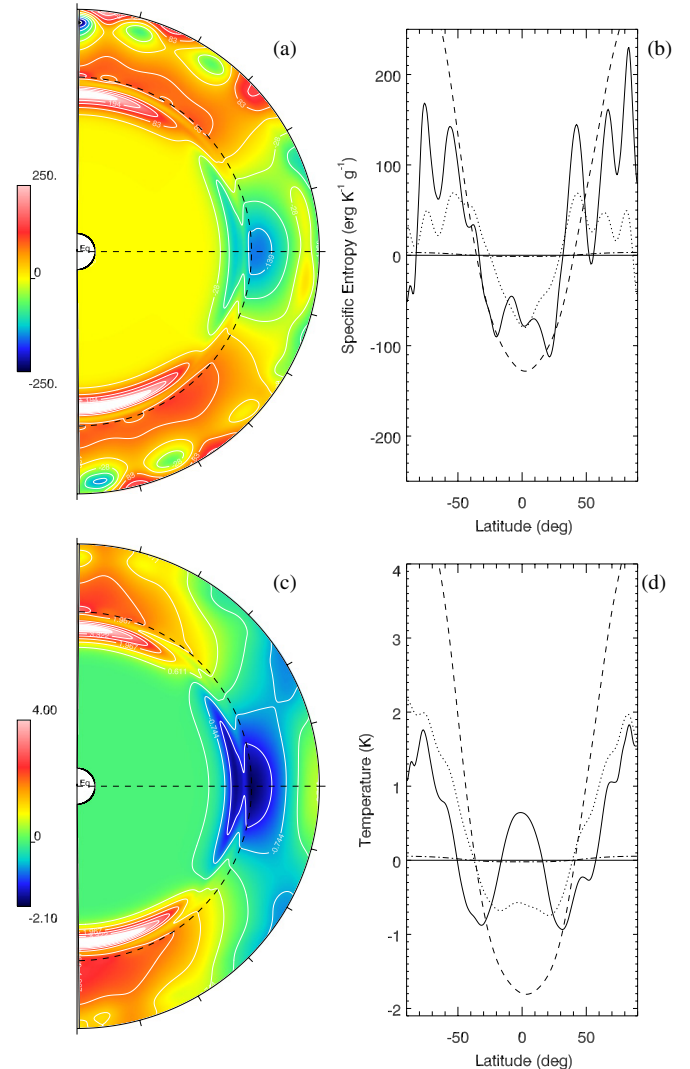
Figure 13. Temporal and azimuthal average of the (a and b) entropy (S) and (c and d) temperature (T) fluctuations realized in the simulations. Shown in the left panels (a and c) are color contours in the full domain and in the right panels (b and d) latitudinal cuts at various depths (solid, dotted, dashed, dash-dotted, three-dot-dashed lines, respectively, at $r = 0.96, 0.85, 0.7, 0.5, 0.3R$). In the left panels the base of the convection zone, $r_{\rm bcz}$, is indicated by a semi-circular dashed line. Clearly evident are the relatively large fluctuations near the base of the convection zone and tachocline, a signature of thermal wind balance (see Section 4.6).

(A color version of this figure is available in the online journal.)

4.5. Meridional Force Balance and Baroclinicity

As published in BAC10, a general meridional balance equation can be derived that reveals the subtle role of all processes in maintaining a non-cylindrical rotation profile that differs from the "classical" thermal wind balance (Durney 1999; BT02; Balbus et al. 2009). It is straightforward to use our numerical simulation to evaluate what are the dominant terms and how this meridional force balance comes about. Let us first recall how such an equation is derived from the vorticity equation:

$$\frac{\partial \boldsymbol{\omega}}{\partial t} = (\boldsymbol{\omega}_a \cdot \boldsymbol{\nabla})\mathbf{v} - (\mathbf{v} \cdot \boldsymbol{\nabla})\boldsymbol{\omega}_a - \boldsymbol{\omega}_a(\boldsymbol{\nabla} \cdot \mathbf{v}) + \frac{1}{\bar{\rho}^2}\boldsymbol{\nabla}\bar{\rho}\boldsymbol{\nabla}P$$
$$- \boldsymbol{\nabla} \times \left(\frac{\rho g}{\bar{\rho}}\hat{\mathbf{e}}_r\right) - \boldsymbol{\nabla} \times \left(\frac{1}{\bar{\rho}}\boldsymbol{\nabla} \cdot \mathcal{D}\right), \quad (11)$$

with $\boldsymbol{\omega}_a = \boldsymbol{\nabla} \times \mathbf{v} + 2\boldsymbol{\Omega_0}$ the absolute vorticity and $\boldsymbol{\omega} = \boldsymbol{\nabla} \times \mathbf{v}$ the vorticity in the rotating frame. Averaging the zonal component of this vorticity equation over longitude and time and assuming a statistically stationary state yields the general equation for force balance in the meridional plane:

$$2\Omega_0 \frac{\partial \langle v_\phi \rangle}{\partial z} = \underbrace{-\left\langle (\boldsymbol{\omega} \cdot \boldsymbol{\nabla}) v_\phi - \frac{\omega_\phi v_r}{r} - \frac{\omega_\phi v_\theta \cot \theta}{r} \right\rangle}_{\text{Stretching}}$$

$$+ \underbrace{\left\langle (\mathbf{v} \cdot \boldsymbol{\nabla}) \omega_\phi + \frac{v_\phi \omega_r}{r} + \frac{v_\phi \omega_\theta \cot \theta}{r} \right\rangle}_{\text{Advection}}$$

$$- \underbrace{\langle \omega_\phi v_r \rangle \frac{d \ln \bar{\rho}}{dr}}_{\text{Compressibility}} + \underbrace{\frac{1}{r} \left[\frac{\partial}{\partial r} (r \langle \mathcal{A}_\theta \rangle) - \frac{\partial}{\partial \theta} \langle \mathcal{A}_r \rangle \right]}_{\text{Viscous stresses}}$$

$$+ \underbrace{\frac{g}{r c_p} \frac{\partial \langle S \rangle}{\partial \theta} + \frac{1}{r \bar{\rho} c_p} \frac{d \bar{S}}{dr} \frac{\partial \langle P \rangle}{\partial \theta}}_{\text{Baroclinicity}} \qquad (12)$$

where $\dfrac{\partial}{\partial z} = \cos \theta \dfrac{\partial}{\partial r} - \dfrac{\sin \theta}{r} \dfrac{\partial}{\partial \theta}$ and

$$\langle \mathcal{A}_r \rangle = \frac{1}{\bar{\rho}} \left\langle \left[\frac{1}{r^2} \frac{\partial (r^2 \mathcal{D}_{rr})}{\partial r} + \frac{1}{r \sin \theta} \frac{\partial (\sin \theta \mathcal{D}_{\theta r})}{\partial \theta} - \frac{\mathcal{D}_{\theta\theta} + \mathcal{D}_{\phi\phi}}{r} \right] \right\rangle,$$

$$\langle \mathcal{A}_\theta \rangle = \frac{1}{\bar{\rho}} \left\langle \left[\frac{1}{r^2} \frac{\partial (r^2 \mathcal{D}_{r\theta})}{\partial r} + \frac{1}{r \sin \theta} \frac{\partial (\sin \theta \mathcal{D}_{\theta\theta})}{\partial \theta} \right] \right.$$
$$\left. + \frac{1}{\bar{\rho}} \left[\frac{\mathcal{D}_{\theta r} - \cot\theta \mathcal{D}_{\phi\phi}}{r} \right] \right\rangle. \qquad (13)$$

In the above equation we have identified several terms.

1. Stretching describes the stretching and tilting of the vorticity due to velocity gradients.
2. Advection describes the advection of vorticity by the flow.
3. Compressibility describes the change of vorticity due to compression.
4. $(g/r c_p)(\partial \langle S \rangle / \partial \theta)$ is the dominant component of the baroclinic term when the stratification is nearly adiabatic.
5. $(1/r \bar{\rho} c_p)(d \bar{S}/dr)(\partial \langle P \rangle / \partial \theta)$ represents baroclinic forcing arising from a finite radial entropy gradient.
6. Viscous accounts for the viscous diffusion of vorticity.

Under the assumption that the convection zone is nearly adiabatic and hydrostatic, that the Rossby number $R_o = \omega / 2\Omega_0$ is small, and that viscous stresses can be neglected, Equation (12) simplifies to give

$$\frac{\partial \langle v_\phi \rangle}{\partial z} = \frac{g}{2\Omega_0 r c_p} \frac{\partial \langle S \rangle}{\partial \theta}. \qquad (14)$$

This is the "classical" thermal wind equation. It states that baroclinicity can break the Taylor–Proudman constraint of $\partial v_\phi / \partial z = 0$, implying a cylindrical rotation profile (Zahn 1992). This is due to the fact that baroclinic torques suppress the Coriolis-induced meridional circulation that would otherwise tend to establish a cylindrical state of rotation. We now turn to our numerical simulation to evaluate the role played by all the terms of the zonal vorticity equation identified above and to discuss the nature of the meridional force balance.
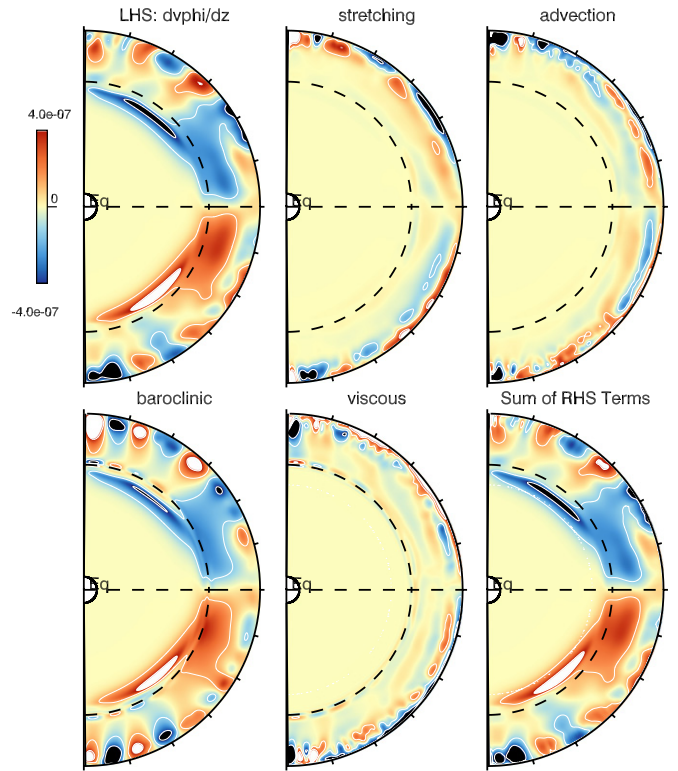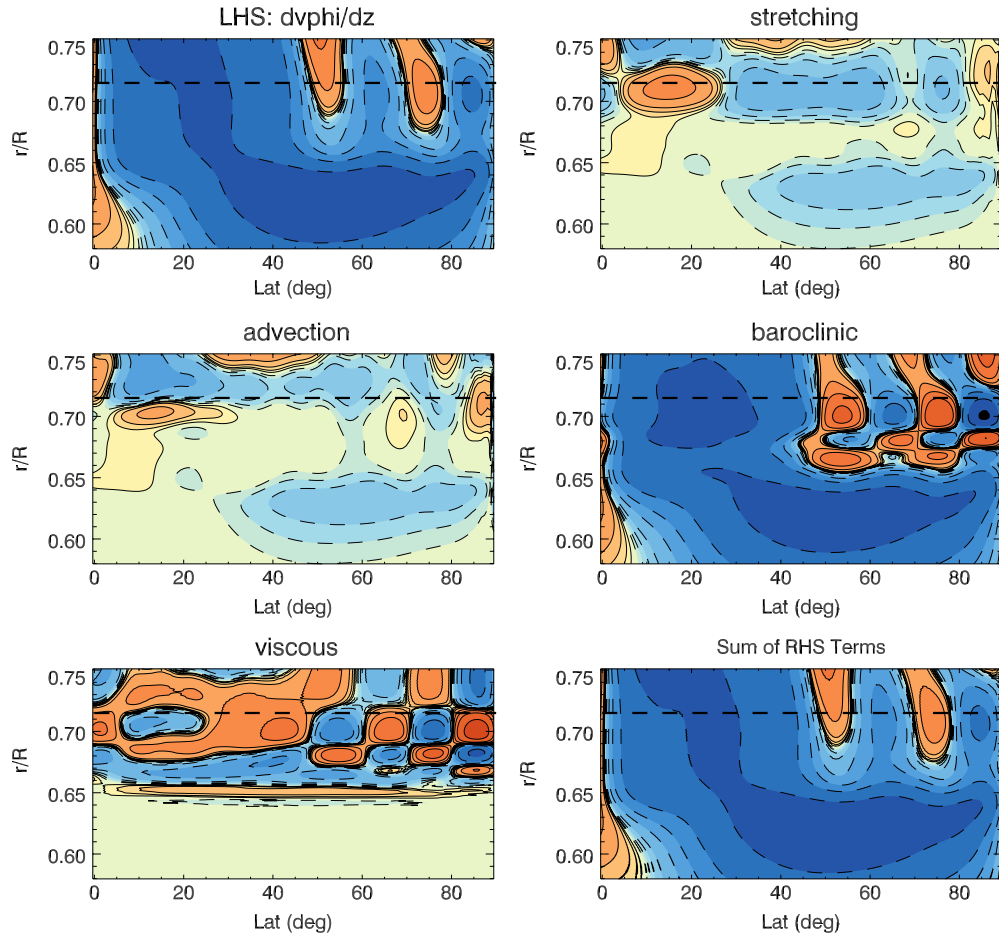

Figure 14. The terms discussed in Equation (12) are shown here, averaged over azimuth and 10 solar rotation periods. Shown are in turn: $\partial \langle v_\phi \rangle / \partial z$, the stretching and advection of vorticity, the baroclinic effects, the viscous stresses, and the sum of the rhs terms (we have divided all the rhs terms by $1/2\Omega_0$). The color scale in all panels saturates at $\pm 4 \times 10^{-7}$ s^{-1}, with red denoting positive values.

(A color version of this figure is available in the online journal.)

Figure 14 displays the lhs and rhs of Equation (12), for our 3D solar model simulation, as well as the dominant components of the rhs. We clearly see that the sum of the rhs term is in very close agreement with the lhs, signifying an approximately steady state over the time period sampled (about 10 rotation periods). Shorter averages are generally less balanced while longer averages change neither the quality of the balance nor the structure or amplitude of the various terms.

Our more detailed decomposition of the vorticity equation allows us to identify which terms are contributing and where. First, the baroclinic term is found to be important in most of the bulk of the convection zone as was found by BT02 and MBT06. We also find that it is the dominant term below the base of the convection zone, in the region of strong shear (i.e., in the tachocline). This is consistent with the presence of strong thermal gradients as discussed in Section 4.4. Advection and stretching terms are found to contribute to the overall balance in multiple places, throughout the bulk of the convection zone as well as near the top and bottom. In contrast to the baroclinic term they do not generally exhibit large-scale structure with one dominant sign in each hemisphere. Without these terms, the agreement between the lhs and the rhs would not be as good. Since the Rossby number realized in the simulation is less than one, we expect the advection and stretching term to be small on average in the simulations and, indeed, their maximum amplitude is not as large as the baroclinic term. However, this is not the case at all scales or at all locations and they do contribute in key places such as near the surface and at mid-latitude in the bulk of the convection zone. Finally, in our model a viscous

Figure 15. Expanded view near the tachocline of the terms discussed in Equation (12) averaged over azimuth and 10 rotation periods. Shown are in turn: $\partial\langle v_\phi\rangle/\partial z$, the stretching and advection of vorticity, the baroclinic effects, the viscous stresses, and the sum of the rhs terms (we have divided all the rhs terms by $1/2\Omega_0$). The color table saturates in each panel at $\pm 10^{-6}$ s^{-1}, with red denoting positive values.

(A color version of this figure is available in the online journal.)

shear layer dominates the balance at the surface where the isocontours of Ω possess the strongest latitudinal shear and also near the base of the convection zone, where the angular velocity profile becomes nearly uniform. Durney (1989) and Kitchatinov & Rüdiger (1999) have also stressed that a strict thermal wind balance cannot be realized everywhere in the convection zone and that turbulent viscous stresses may play a role near the boundaries as observed in Figure 14.

From our analysis of the full meridional balance, we can conclude that Equation (14) is only partly satisfied in the convection zone of our 3D simulations. Clearly, baroclinic effects play a central role but these are far from being dominant everywhere, and considering only Equation (14) instead of the full balance expressed in Equation (12) would be misleading in the convective envelope. Let us now evaluate how well the traditional thermal wind balance at the base of the convection is realized, since the baroclinic term seems to be the main player there.

In Figure 15 we show again the main contributions to the meridional balance equation but zoomed between 0.58 and 0.75R and only in the northern hemisphere. Here the subtle balance realized in that complex transition layer becomes clear. We note that below about 0.65R the baroclinic term is totally dominant, helped only slightly by the advection and stretching terms. At such depth we are actually below the base of the overshoot region (r_o), and motions here are only driven by the

downward spread of the tachocline in our model as discussed in Brun & Zahn (2006). Above that radius a more complex balance is operating involving all terms. In the polar region, many structures with alternating signs are present in most terms, with the baroclinic and viscous terms having mostly opposite signs. At the pole we thus do not get an exact baroclinic balance in our model. This is more true at low latitudes where the contributions of the viscous, advection and stretching terms compensate more or less one another, leaving the baroclinic term as the only main contributor.

5. COUPLING BETWEEN CONVECTIVE AND RADIATIVE ZONES

Understanding and quantifying how angular momentum is transported between the convection zone and the radiative zone is of essential importance in interpreting and modeling the rotational evolution of late-type stars as discussed in Section 1.2 (Gilman et al. 1989; Denissenkov et al. 2010; Spada et al. 2010). Our simulation provides an unprecedented opportunity to explore this within the context of a 3D dynamical convection model.

5.1. Tachocline Spreading

In Section 4.3, we emphasized the role of gyroscopic pumping in maintaining the meridional circulation in the convection zone.
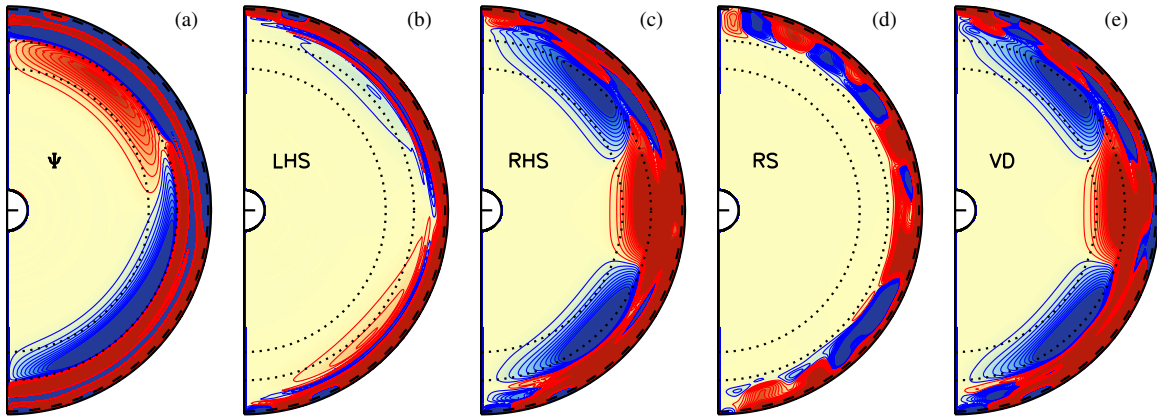
Figure 16. Similar to Figure 12 but emphasizing the radiative zone, with all plots limited to $r \leqslant 0.72R$ and with the mass flux stream function plotted in frame (a) with red and blue denoting clockwise and counterclockwise circulations, respectively. Here the radial and latitudinal angular momentum transport by the Reynolds stresses (RSs) have been combined into a single frame (d) (e.g., with $RS = RS_r + RS_\theta$). Frames (b) and (c) represent the left- and right-hand sides of Equation (8), as in frames (a) and (b) of Figure 12. Frame (e) in both figures is the contribution to the right-hand side from viscous diffusion. As in Figure 12, red and blue in frames (b)–(d) denote positive and negative values but the saturation level of the color table is lower: $\pm 9.10 \times 10^4$ erg cm^{-3}. Typical flow amplitudes in (a) range from 2–3 m s^{-1} at the base of the convection zone to 2.5×10^{-8} m s^{-1} at a radius of $r = 0.5R$. The dashed line indicates the base of the convection zone at $r = 0.71R$ and dotted lines indicate radii of $0.5R$ and $0.6R$ for reference.

(A color version of this figure is available in the online journal.)

Here we note that although the Reynolds stresses responsible for maintaining the differential rotation and meridional circulation are confined principally to the convection zone, the flows themselves need not be. The nature of gyroscopic pumping is such that a localized torque $\mathcal{T}$ can induce a global meridional flow (Haynes et al. 1991). Within the context of solar-type stars, this implies that the maintenance of differential rotation by Reynolds stresses in the convective envelope can induce a meridional flow that spreads downward into the radiative interior (Spiegel & Zahn 1992; Gough & McIntyre 1998; Brun & Zahn 2006; McIntyre 2007; Garaud & Acevedo Arreguin 2009). If turbulent and diffusive stresses are negligible in the radiative interior, then $\mathcal{T} \approx 0$ and the induced circulation follows isosurfaces of $\mathcal{L}$.

The downward burrowing of the gyroscopically pumped meridional circulation and the associated spreading of the tachocline is mediated by the radiative diffusion and operates on an Eddington–Sweet timescale:

$$\tau_{\mathrm{ES}} = \left(\frac{N}{2\Omega_0} \right)^2 \frac{r_{\mathrm{bcz}}^2}{\kappa} . \tag{15}$$

In the Sun $\tau_{\mathrm{ES}} \sim 2 \times 10^{11}$ yr, although significant spreading (down to $0.3R$) is expected to occur over the Sun's current lifetime of 4.6 billion yr (Spiegel & Zahn 1992).

The Eddington–Sweet timescale in our simulation is much shorter due to the relatively large value of the thermal diffusivity κ, yielding $\tau_{\mathrm{ES}} \sim 8 \times 10^5$ yr (for $N \sim 4 \times 10^{-4}$ s^{-1}). Viscous diffusion also contributes to the spreading of the tachocline, operating on a timescale of $\tau_d = r_{\mathrm{bcz}}^2/\nu \sim 940$ yr. Thus, we expect viscous spreading to dominate over radiative spreading in our simulation. Furthermore, since both spreading timescales are longer than the duration of the simulation, we expect that the tachocline has not reached a steady state and is instead slowly diffusing downward. This is consistent with the analysis by Brun & Zahn (2006) who show that viscous spreading of the tachocline dominates over thermal spreading when the Prandtl number is greater than 10^{-3}.

This is indeed the case, as demonstrated in Figure 16. Here we see that the Reynolds stress is negligible below about

$r = 0.6R$ (Figure 16(d)) where the net torque (Figure 16(c)) is dominated by the viscous term (Figure 16(e)). In contrast to the convection zone, the advection of angular momentum by the meridional circulation (Figure 16(b)) does not balance the net torque (Figure 16(c)) so the dynamical balance expressed in Equation (8) is not satisfied. Rather, viscous torques are speeding up the equator relative to the poles as the differential rotation in the convection zone spreads downward.

The meridional circulation in the stable zone exhibits a complex-layered structure with multiple cells in radius (Figure 16(a)). The latitudinal structure is dominated by one cell per hemisphere of opposite senses but there is significant flow across the equator, indicating that the spreading of the tachocline is not symmetric. Near the leading edge of the spreading front at $r \sim 0.5R$, there is a very weak poleward circulation with an amplitude less than 10^{-7} m s^{-1}. Here viscous torques slow the rotation rate and induce a flow toward the rotation axis by means of the Coriolis force. Buoyancy tends to restrict the flow to horizontal surfaces but mass conservation requires downflow near the equator and upflow near the poles. At $r = 0.6R$ and at the base of the convection zone ($r = 0.71R$) the flow is predominantly equatorward. However, there is a region of poleward flow in between at $r \sim 0.64R$, so there are four layered circulation cells.

5.2. Implications for Tachocline Confinement

The narrow extent of the present-day tachocline inferred from helioseismology implies that some physical mechanism is inhibiting the radiative spreading and thus confining the tachocline. Possible mechanisms include anisotropic turbulence (Spiegel & Zahn 1992; Elliott 1997), magnetic torques (Rüdiger & Kitchatinov 1997; Gough & McIntyre 1998), and internal waves (Charbonnel & Talon 2005; Rogers & Glatzmaier 2006). The magnetic confinement models of Rüdiger & Kitchatinov (1997) and Gough & McIntyre (1998) attribute tachocline confinement to a fossil magnetic field embedded in the radiative interior of the Sun since its formation. Alfvénic torques can maintain uniform rotation in the radiative interior but only if they form closed poloidal configurations that avoid the differential rotation of the convective envelope (MacGregor & Charbonneau 1999; Brun & Zahn 2006; Strugarek et al. 2011).

The simulation reported here exhibits anisotropic flows in the tachocline and internal gravity waves, but these are insufficient to halt the spread of the tachocline. However, we cannot conclusively rule these out as plausible tachocline confinement mechanisms. Although the viscous torques that dominate the tachocline spreading in our simulation are much smaller than in the convection zone, they are still many orders of magnitude larger than the viscous torques in the Sun. Furthermore, the resolution of our simulation may be insufficient to reliably capture angular momentum transport by stably stratified turbulence and waves. As our simulation is non-magnetic, we cannot directly address magnetic confinement mechanisms. MHD analogs of this simulation are currently underway and have been reported in Strugarek et al. (2011). Still, the nature of the meridional circulation in the simulation reported here does have implications for magnetic tachocline confinement models.

Gyroscopically pumped meridional flows have been proposed as a mechanism for keeping fossil fields localized within the radiative interior, making magnetic confinement feasible (Gough & McIntyre 1998; Garaud 2002; McIntyre 2007; Wood & McIntyre 2011). Models that rely on this mechanism are particularly sensitive to the structure of the flow at high latitudes. Any axisymmetric meridional flow must be strictly vertical at the poles, so the latitudinal flow required for confinement of the fossil field to the radiative zone must be established very close to the rotation axis to avoid a "polar pit" where the circulation and in turn the rotational shear spreads deep below the convection zone (McIntyre 2007). In the recent confinement model by Wood & McIntyre (2011), a retrograde torque $\mathcal{T} < 0$ in the convection zone induces a meridional flow via gyroscopic pumping that converges on the rotation axis and then turns downward. As this downward meridional flow encounters the fossil field in the radiative interior, it is diverted equatorward by the Lorentz force, forming a steady, axisymmetric, magnetostrophic boundary layer that pins down the fossil field. However, Strugarek et al. (2011) found that in the parameter regime they studied the meridional circulation cannot prevent the spread of the tachocline. They find that the field is advected into the convection zone, establishing Ferraro's law of iso-rotation in the radiative interior. Recent 2D studies by Rogers (2011) also reports that the field is not confined by the meridional flow. However, in their case the angular momentum transport by magnetic stresses is much less efficient and the radiative interior maintains a solid body rotation. In any case, the temporally varying meridional flows driven by the convection zone seem to play an important role in determining whether or not this flow can or cannot confine the field such that this fossil field can prevent the inward spread of the tachocline.

In our simulation, the low-latitude convergence of angular momentum due to the convective Reynolds stress is sustained by means of a mid-latitude divergence (Figure 12(d)). In other words, it is the transport of angular momentum from mid to low latitudes that maintains the differential rotation in the convection zone. This is in part a consequence of geometry: the polar regions account for only a small fraction of the integrated angular momentum in the system so their role in sustaining a fast prograde rotation at low latitudes is severely limited. Furthermore, the relatively small volume and the small moment arm in the polar regions give rise to large temporal fluctuations in the rotation rate Ω and the net torque $\mathcal{T}$. Over the 10 solar periods averaging intervals shown in Figures 10 and 12, the values of both Ω and $\mathcal{T}$ (relative to the rotating coordinate system) near the base of the convection zone have opposite signs at the north

and south poles. Yet, apart from these transient fluctuations, the mean angular velocity largely decreases monotonically from equator to pole.

The high-latitude fluctuations in $\mathcal{T}$ and Ω within the convection zone induce similar fluctuations in the meridional flow. Despite the large time variations, the gyroscopic pumping of Equation (8) is still approximately satisfied near the poles (Figures 12(a) and (b)). However, the absence of a systematic retrograde torque gives rise to a meridional flow structure with multiple high-latitude cells of varying orientations. The time period covered in Figures 11 and 12, for example, exhibits an asymmetric series of two to three countercells in each hemisphere which culminate in a downward flow at the north pole and an upward flow at the south pole.

The weak circulations below the convection zone are less variable but exhibit a layered structure of four cells as noted above (Figure 16(a)). Proceeding downward from the base of the convection zone at the poles, one encounters regions of downflow, upflow, downflow, and upflow. The detailed flow structure is likely sensitive to the stratification, the viscosity and diffusivity profiles, and other factors such as Reynolds and Prandtl numbers. Magnetic fields may also alter the nature of the circulation and the coupling between the radiative zone and the convection zone.

To summarize the implications for tachocline confinement, there is little indication of a prominent, persistent divergence in the convective angular momentum transport at high latitudes, which would give rise to a retrograde torque and a steady polar downwelling as in the model of Wood & McIntyre (2011). A persistent retrograde high-latitude torque may emerge from longer time averages, but it is still likely to be weak relative to lower-latitude torques. This is a consequence not only of the geometry but also of the nature of rotating turbulent convection. At high latitudes where the rotation vector is nearly vertical, the convection structure is dominated by helical downflow plumes with a small horizontal extent (Julien et al. 1996; Brummell et al. 1996; Miesch et al. 2000, 2008). Although the plumes exhibit systematic tilts toward the rotation axis due to turbulent alignment, the associated latitudinal angular momentum transport by the Reynolds stress, namely $\lambda \bar{\rho} \langle v'_\theta v'_\phi \rangle$, is minimal relative to Coriolis-induced Reynolds stresses at lower latitudes. Whether such a weak, time-varying torque in the polar regions can support a boundary layer of the type envisioned by Wood & McIntyre requires further research. Furthermore, the robustness of the layered circulation cells exhibited in Figure 16(a) warrants further investigation, particularly for parameter regimes where thermal (radiative) spreading prevails over viscous spreading.

5.3. Rotational Coupling

In order to assess the net coupling between the convection zone and the radiative zone, we define the integrated angular momentum flux across a horizontal surface as follows:

$$I(r, t) = 2\pi r^2 \int_0^\pi \mathcal{F}_r(r, \theta, t) \sin\theta \, d\theta, \qquad (16)$$

where $\mathcal{F}_r$ has Reynolds stress and viscous components as expressed in Equation (10). Note that here we define $\mathcal{F}_r$ through a longitudinal average alone whereas in Section 4.3 we also averaged over time. In a similar manner, we also define the integrated flux across a horizontal surface arising from the advection of angular momentum by the meridional circulation. Results are shown in Figure 17.
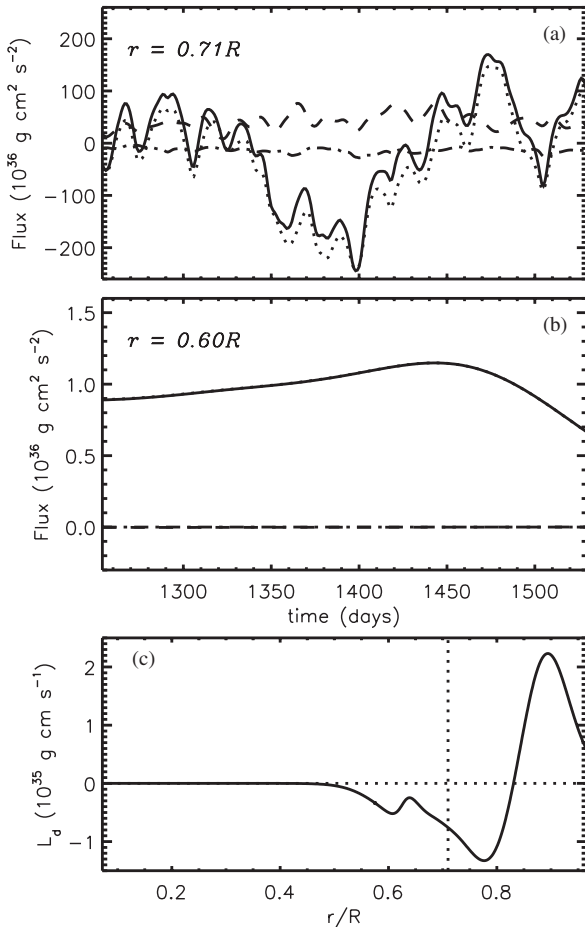
Figure 17. Integrated angular momentum flux $I(r,t)$ across horizontal surfaces located (a) at the base of the convection zone, $r = 0.71R$, and (b) at $r = 0.6R$ as a function of time. Shown are contributions from the Reynolds stress (dot-dashed lines), the viscous diffusion (dotted lines), and the meridional circulation (dashed lines). The sum of all three contributions is also shown (solid line). The time interval corresponds to the averages shown in Figures 12 and 16. Panel (c) shows the change in angular momentum vs. radius (Equation (17)) at $t = 1528$ days. Vertical dotted line indicates the base of the convection zone and the horizontal dotted line indicates the initial condition of uniform rotation.

The angular momentum transport by the meridional circulation across the base of the convection zone is outward, tending to slow down the rotation of the radiative zone, while the weaker Reynolds stresses transport angular momentum inward (Figure 17(a)). The net viscous transport is both larger on average and more variable, reversing sign several times over the 275 day time interval shown. Deeper down, viscous transport dominates the spreading of the tachocline and is predominantly outward, extracting angular momentum from the quiescent interior (Figure 17(b)).

Recall that the boundary conditions are stress free so the total angular momentum in the simulation is conserved (Section 4.3). Angular momentum that is extracted from the radiative zone, primarily by viscous stresses, is transported to the upper convection zone, as demonstrated in Figure 17(c). This shows the change in angular momentum relative to the initial condition, integrated over horizontal surfaces:

$$L_d(r, t) = 2\pi r^2 \int_0^\pi \bar{\rho}\,(\mathcal{L} - \mathcal{L}_0)\sin\theta\,d\theta, \qquad (17)$$

where $\mathcal{L}$ is defined in Equation (9) and $\mathcal{L}_0 = \lambda^2\Omega_0$.

In an actual star, the angular momentum in the convection zone will decrease with time due to external torques from a magnetized wind and this will be transmitted to the radiative zone by circulations, waves, instabilities, or Lorentz forces. It is notable that the convection zone in our simulation is extracting angular momentum from the radiative zone despite the absence of a stellar wind. The timescale for this extraction is short relative to spin-down timescales. The initial angular momentum in the radiative zone of our simulation is obtained by integrating $\bar{\rho}\mathcal{L}_0$ over the volume between the bottom boundary and the base of the convection zone, yielding a value of $L_{RZ} = 1.9 \times 10^{48}$ g cm^2 s^{-1}. If we divide this by a typical flux amplitude in Figure 17(b) of 10^{36} g cm^2 s^{-2}, we obtain a coupling timescale of approximately 6×10^4 yr. Since the flux across a given surface varies with time, a better estimate of the coupling timescale can be obtained by calculating $\tau_c \sim L_{RZ}\Delta t/\Delta L$, where Δt is the simulation time of 1528 days and ΔL is the integral of L_d shown in Figure 17(c) over the radiative zone. This yields $\tau_c \sim 1.6 \times 10^4$ yr. Including the volume below our inner boundary increases these values by only about a tenth of a percent.

These estimates for the rotational coupling timescale likely underestimate true solar and stellar values, given the relatively large viscous diffusion in our simulation. Indeed, 1D models and stellar observations suggest longer coupling timescales, ranging from 10^6 to 10^8 yr (Irwin et al. 2008; Denissenkov et al. 2010) and spin-down timescales of the order of a few 10^8 yr. Both estimates are consistent with the solar internal rotation profile inferred from helioseismology, according to which the uniform rotation rate of the radiative interior is intermediate between the equatorial and polar rotation rates of the convection zone (Thompson et al. 2003). The sensitivity of helioseismic inversions is consistent with almost no net viscous torque across the tachocline, implying rapid dynamical equilibration relative to the spin-down timescale of the convective envelope (Gilman et al. 1989).

Note that we do not attribute the coupling between the convection and radiative zones in the Sun to molecular viscosity. Extrapolating the coupling timescale found here to the molecular viscosity of the solar plasma would imply timescales far longer than those suggested by solar and stellar observations. However, some SGS transport mechanisms may act effectively as a turbulent diffusion. Examples include intermittent shear instabilities that can occur even in a nominally stable stratification (e.g., Fritts et al. 2003) or small-scale Maxwell stresses that resist rotational shear by means of magnetic tension. Thus, our transport may be regarded as an effective turbulent diffusion which, although still larger than the stellar value, may yet be consistent with observations of stellar spin-down. If, on the other hand, the coupling between the solar convection zone and the radiative interior is achieved by essentially non-diffusive processes such as wave transport or large-scale magnetic torques, then the coupling mechanism we see in our simulation is likely not applicable to the Sun. More importantly, we note that the tachocline in our simulation is spreading downward (cf. Section 5.1), which does not appear to be the case in the Sun. Whatever mechanism confines the tachocline likely also regulates the rotational coupling between the convection and radiative zones. Until more is known about this mechanism, coupling estimates such as those presented in this section should be regarded as illustrative but tentative.

6. DISCUSSION AND PERSPECTIVES

In this paper, we have presented the first 3D model of the Sun from $r = 0.07$ up to $0.97R$ that uses a realistic stratification in

the radiative interior and couples nonlinearly the convection and radiation zones. This simulation is extremely rich and instructive with regard to the inner dynamics of the Sun. It exhibits a wide range of complex physical processes including turbulent convection, penetration, internal wave generation, large-scale flows, and tachocline dynamics.

Compared with our previous results that considered only the convective envelope (e.g., Elliott et al. 2000; Brun & Toomre 2002; Miesch et al. 2008), the presence of a stable radiative interior at the base of the convective zone promotes a differential rotation profile that it is in good agreement with helioseismic rotational inversions, even if a bit weaker (Thompson et al. 2003). We find that as anticipated in Rempel (2005) and MBT06, the existence of a subadiabatic layer below the convective envelope influences greatly the differential rotation established in the convection zone. Anisotropic heat transport and meridional circulations near the base of the convection zone establish larger temperature and entropy gradients than otherwise found in purely convective models and the resulting baroclinic torques break the Taylor–Proudman constraint of a cylindrical (quasi-2D) differential rotation profile. A detailed study of the meridional force balance indicates that the classical thermal wind balance is fully realized in the stable layer below, whereas some departure mostly due to Reynolds stresses are found in the convective envelope. Strong differential rotation leads naturally to the establishment of a tachocline of shear near the base of the convective envelope. We began the simulation with uniform rotation in the radiative interior and the tachocline develops as a transition layer linking the convective and radiative zones. This is the first time that a tachocline has been established self-consistently in a 3D simulation of solar convection without imposing any ad hoc forcing, and as such, constitutes a notable breakthrough.

The realistic solar stratification establishes a thin overshoot region at the base of the convection zone where downflow plumes are buoyantly decelerated. The base of the convection zone ($r_{bcz} = 0.715R$) as defined by a sign reversal of the longitudinally averaged radial entropy gradient, $\partial(\langle S \rangle + \overline{S})/\partial r$, exhibits no significant latitudinal variation. However, the top (r_c) and bottom (r_o) of the overshoot region as quantified by the enthalpy flux are both slightly prolate, indicating more efficient overshoot at low latitudes (Figure 7). The latitudinal variation of r_c (0.725R–0.742R) is greater than that of r_o (0.672R–0.678R) so the thickness of the mixing region varies with latitude. Enhanced overshoot at low latitudes may be attributed to the "flywheel" action of rotationally aligned convective columns (banana cells) which efficiently burrow inward near the tangent cylinder (Brummell et al. 2002). The distance from the base of the convection zone ($r_{bcz} = 0.715R$) to the bottom of the overshoot region ($r_o = 0.672R$–0.678R) is about 0.04R, or about half of the pressure scale height $H_P = 0.08R$, in agreement with the value quoted by Rogers & Glatzmaier (2006) in their 2D equatorial study. This is smaller than in previous global 3D convection simulations but more than theoretical estimates of the penetration depth which are less than 0.01R (Zahn 1991; Rempel 2004). The discrepancy is likely due to the laminar nature of our convective motions; turbulent convective plumes are expected to occupy a smaller filling factor, inhibiting overshoot. Recent estimates of the extent of convective overshoot in the Sun based on helioseismic inversions and semi-analytic modeling of turbulent plumes suggest a penetration depth of ∼0.03R, only slightly less than in our model (Christensen-Dalsgaard et al. 2011).

Another interesting aspect of this simulation, warranting further analysis that we defer to a subsequent paper, is the generation of internal waves by the penetrative convective motions. Here again for the first time a full 3D view of internal wave excitation and propagation in a global simulation of the Sun is achieved. We find that these waves propagate mostly horizontally, as expected given the strong vertical stratification. A large spectrum of waves is continuously excited by the pummeling of convective motions. Clearly near the base of the convection envelope large perturbations are found, upon which smaller-amplitude wave motions spanning the entire radiative interior are superimposed. Animations reveal wave patterns that spiral outward, implying an outward phase velocity.

We have also presented a novel analysis of the maintenance of the meridional circulation based on the concept of gyroscopic pumping. The main objective of this analysis is to elucidate the coupling between the convection and radiative zones but it also provides insight into the maintenance of the circulation in the convection zone itself. The meridional circulation profile is dominated by a single cell in each hemisphere, with equatorward flow near the base of the convection zone and poleward flow in the upper convection zone. This is attributed mainly to zonal torques associated with equatorward and inward angular momentum transport at mid-latitudes (Figure 12). As in previous simulations of global solar convection, transient, multi-celled meridional circulations with large fluctuation with respect to the mean are present, requiring long temporal averages, of at least several months, to reveal persistent flows (e.g., Miesch & Toomre 2009). The amplitude of the meridional circulation drops off rapidly below the convection zone, from a few m s^{-1} at $r = 0.71R$ to a few mm s^{-1} by $0.67R$.

In idealized axisymmetric models of the solar tachocline, the combined influence of gyroscopic pumping, thermal wind balance, and radiative diffusion gives rise to a spreading of the tachocline on a timescale of the order of 10^9 yr (Spiegel & Zahn 1992; Gough & McIntyre 1998). The tachocline is indeed spreading inward in our simulation but not in the manner advocated by these models. Instead, the spread of the tachocline is governed mainly by viscous diffusion and occurs on a shorter timescale, of order 10^3 yr (Section 5.1). Since the viscous diffusion in our simulation is artificial, the detailed structure of the spreading front should be interpreted with caution. Even so, some results may be robust to alternate transport mechanisms that operate locally and that are not captured in our model, such as Reynolds and Maxwell stresses associated with small-scale turbulence. For example, the viscous spread of the tachocline extracts angular momentum from the radiative interior and deposits it in the upper convection zone (Figure 17). This can be attributed to the prograde differential rotation in the convection zone coupled with the conservation of angular momentum in the simulation, resulting in an inward gradient Ω at high latitudes that exceeds the outward gradient at low latitudes. Thus, a similar extraction of angular momentum from the core is expected from any local transport mechanism that, like turbulent diffusion, scales with $\nabla\Omega$. The coupling timescale between the convection and radiative zones is of the order of 10^4 yr, several orders of magnitude less than suggested by stellar observations but about five orders of magnitude larger than convective timescales.

In the magnetic tachocline confinement model of Gough & McIntyre (1998), a fossil magnetic field in the radiative interior offsets the spreading, establishing a steady boundary layer in which the downward advection of angular momentum by the

gyroscopically pumped circulation is balanced by the Lorentz force. The viability of this scenario is very sensitive to the structure of the circulation at high latitudes, as recently emphasized by Wood & McIntyre (2011). In particular, Wood & McIntyre propose that a polar downwelling maintained by a high-latitude divergence of the convective angular momentum flux prevents the fossil field from threading the convection zone and thereby disrupting the boundary layer. Our simulation does not support this scenario. Instead, we find multiple layered circulation cells below the convection zone with polar *upwellings* near the leading edge of the spreading tachocline front (Figure 16). This too can be understood as arising from gyroscopic pumping, responding to retrograde viscous torques at mid-latitudes. Furthermore, it is subject to the caveat noted above, namely that artificial viscous diffusion dominates the structure of the spreading tachocline front. Still, despite the solar-like differential rotation profile, the simulation does not exhibit the strong, persistent, retrograde torques at high latitudes required to sustain a prominent polar downwelling through gyroscopic pumping.

This model is a first step toward a more complete unified picture of solar interior dynamics. It exhibits interesting and novel aspects of the nonlinear coupling between the convection zone and the radiative interior but, like all global models, it involves simplifications and tradeoffs. First, this model does not have sufficient spatial resolution to capture small-scale, anisotropic turbulence in the tachocline and its potential role in tachocline confinement as modeled by Spiegel & Zahn (1992), Elliott (1997), and Miesch (2003). Second, we have neglected magnetism in order to establish a baseline for future study. Magnetism is expected to be an essential ingredient of tachocline dynamics, in terms of both the solar dynamo and tachocline confinement. We expect that the addition of magnetic fields will promote the generation of strong toroidal flux structures near the base of the convection zone as in Browning et al. (2006) and Ghizaru et al. (2010), and we intend to investigate the dynamics of such structures within the context of the solar activity cycle and flux emergence. Similarly we have started to take into account the influence of an inner fossil magnetic field on the solar interior dynamics (Strugarek et al. 2011) and find that the confinement of the tachocline by a large-scale fossil magnetic is not easy to realize in the parameters regime explored. Of course our results are likely sensitive to the amplitudes and profiles chosen for our diffusivities, and thus we have sought to be cautious in our deductions about mixing and wave generation. Our numerical simulations should be viewed as simplified experimental settings in which we can now test a number of nonlinear processes that we believe are occurring in concert deep within a star, thus providing a means to help unravel some of the complex dynamics proceeding within the real Sun.

REFERENCES

Balbus, S., Bonart, J., Latter, H., & Weiss, N. O. 2009, MNRAS, 400, 176
Baliunas, S. L., Donahue, R. A., Soon, W. H., et al. 1995, ApJ, 438, 269
Basu, S., & Antia, H. M. 2001, MNRAS, 324, 498
Belkacem, K., Samadi, R., Goupil, M. J., et al. 2009, A&A, 494, 191
Bessolaz, N., Zanni, C., Ferreira, J., Keppens, R., & Bouvier, J. 2008, A&A, 478, 155
Bouvier, J. 2008, A&A, 489, L53
Browning, M. K., Brun, A. S., & Toomre, J. 2004, ApJ, 601, 512
Browning, M. K., Miesch, M. S., Brun, A. S., & Toomre, J. 2006, ApJ, 648, L157
Brummell, N. H., Clune, T., & Toomre, J. 2002, ApJ, 570, 825
Brummell, N. H., Hurlburt, N. E., & Toomre, J. 1996, ApJ, 473, 494
Brun, A. S., Antia, H. M., & Chitre, S. M. 2010, A&A, 510, 33 (BAC10)
Brun, A. S., Antia, H. M., Chitre, S. M., & Zahn, J.-P. 2002, A&A, 391, 725
Brun, A. S., Miesch, M. S., & Toomre, J. 2004, ApJ, 614, 1073
Brun, A. S., & Rempel, M. 2008, Space Sci. Rev., 144, 151
Brun, A. S., & Toomre, J. 2002, ApJ, 570, 865 (BT02)
Brun, A. S., Turck-Chièze, S., & Zahn, J. P. 1999, ApJ, 525, 1032
Brun, A. S., & Zahn, J.-P. 2006, A&A, 457, 665
Busse, F. H. 2002, Phys. Fluids, 14, 1301
Campos, L. M. B. C. 2010, MNRAS, 410, 717
Cayrel, G. 1998, Space Sci. Rev., 84, 145
Chan, K. 2010, in Proc. Symp. 271, Astrophysical Dynamics: From Stars to Galaxies, ed. N. Brummell, A. S. Brun, M. Miesch, & Y. Ponty (Cambridge: Cambridge Univ. Press), 317
Charbonneau, P. 2010, Living Rev. Sol. Phys., 7, 3
Charbonneau, P., Christensen-Dalsgaard, J., Henning, R., et al. 1999, ApJ, 527, 445
Charbonneau, P., & MacGregor, K. B. 1993, ApJ, 417, 762
Charbonnel, C., & Talon, S. 2005, Science, 5744, 2189
Christensen-Dalsgaard, J., Monteiro, M. J. P. F. G., Rempel, M., & Thompson, M. J. 2011, MNRAS, 414, 1158
Clayton, D. D. 1968, Principles of Stellar Evolution and Nucleosynthesis (Chicago, IL: Chicago Univ. Press)
Clune, T. L., Elliott, J. R., Glatzmaier, G. A., Miesch, M. S., & Toomre, J. 1999, Parallel Comput., 25, 361
Corbard, T., Blanc-Féraud, L., Berthomieu, G., & Provost, J. 1999, A&A, 344, 696
Cox, J. P., & Giuli, R. T. 1968, Principles of Stellar Structure (New York: Gordon & Breach)
Denissenkov, P., Schuler, C., Hobbs, L., & Pinsonneault, M. 2010, ApJ, 716, 1269
Durney, B. R. 1989, ApJ, 338, 509
Durney, B. R. 1999, ApJ, 511, 945
Eff-Darwich, A., Korzennik, S. G., Jiménez-Reyes, S. J., & García, R. A. 2008, ApJ, 679, 1636
Elliott, J. R. 1997, A&A, 327, 1222
Elliott, J. R., Miesch, M. S., & Toomre, J. 2000, ApJ, 533, 546
Fritts, D. C., Bizon, C., Werne, J. A., & Meyer, C. K. 2003, J. Geophys. Res., 108, 8452
Garaud, P. 2002, MNRAS, 329, 1
Garaud, P., & Acevedo Arreguin, L. 2009, ApJ, 704, 1
Garaud, P., & Brummell, N. H. 2008, ApJ, 674, 498
Garcia, R. A., Turck-Chize, S., Jimnez-Reyes, S. J., et al. 2007, Science, 316, 1591
Garcia Lopez, R. J., & Spruit, H. C. 1991, ApJ, 377, 268
Ghizaru, M., Charbonneau, P., & Smolarkiewicz, P. K. 2010, ApJ, 715, L133
Gilman, P. A., & Miesch, M. S. 2004, ApJ, 611, 568
Gilman, P. A., Morrow, C., & DeLuca, E. 1989, ApJ, 338, 528
Glatzmaier, G. A. 1984, J. Comp. Phys., 55, 461
Glatzmaier, G. A. 1985, Geophys. Astrophys. Fluid Dyn., 31, 137
Glatzmaier, G. A. 1987, in The Internal Solar Angular Velocity, ed. B. R. Durney & S. Sofia (Dordrecht: Reidel), 263
Glatzmaier, G. A., & Gilman, P. 1982, ApJ, 256, 316
Goldreich, P., & Kumar, P. 1990, ApJ, 363, 694
Gough, D. O., & McIntyre, M. 1998, Nature, 394, 755
Haynes, P. H., Marks, C. J., McIntyre, M. E., Shepherd, T. G., & Shine, K. P. 1991, J. Atmos. Sci., 48, 651
Hurlburt, N. E., Toomre, J., & Massaguer, J. 1986, ApJ, 311, 563
Hurlburt, N. E., Toomre, J., Massaguer, J., & Zahn, J.-P. 1994, ApJ, 421, 245
Irwin, J., Hodgkin, S., Aigrain, S., et al. 2008, MNRAS, 383, 1588
Julien, K., Legg, S., McWilliams, J., & Werne, J. 1996, J. Fluid Mech., 322, 243
Keppens, R., MacGregor, K. B., & Charbonneau, P. 1995, A&A, 294, 469
Kim, E.-J., & Leprovost, N. 2007, A&A, 468, 1025

Kiraga, M., Jahn, K., Stepien, K., & Zahn, J.-P. 2003, Acta Astron., 53, 321
Kitchatinov, L. L., & Rüdiger, G. 1995, A&A, 299, 446
Kitchatinov, L. L., & Rüdiger, G. 1999, A&A, 344, 911
Macgregor, K. B., & Charbonneau, P. 1999, ApJ, 519, 911
Mathis, S., & de Brye, N. 2011, A&A, 526, 65
Mathis, S., Talon, S., Pantillon, F.-P., & Zahn, J.-P. 2008, Sol. Phys., 251, 101
Matt, S., & Pudritz, R. E. 2005, MNRAS, 356, 167
McIntyre, M. E. 1998, Prog. Theor. Phys. Suppl., 130, 137 (corrigendum 101, 189 [1999])
McIntyre, M. E. 2007, in The Solar Tachocline, ed. D. W. Hughes, R. Rosner, & N. O. Weiss (Cambridge: Cambridge Univ. Press), 183
Michaud, G., & Charbonneau, P. 1991, Space Sci. Rev., 57, 1
Michaud, G., & Zahn, J. P. 1998, Theor. Comput. Fluid Dyn., 11, 183
Miesch, M. S. 2003, ApJ, 586, 663
Miesch, M. S. 2005, Living Rev. Sol. Phys., 2, 1
Miesch, M. S., Brun, A. S., DeRosa, M. L., & Toomre, J. 2008, ApJ, 673, 557
Miesch, M. S., Brun, A. S., & Toomre, J. 2006, ApJ, 641, 618 (MBT06)
Miesch, M. S., Elliott, J. R., Toomre, J., et al. 2000, ApJ, 532, 593
Miesch, M. S., & Toomre, J. 2009, Annu. Rev. Fluid Mech., 41, 317
Palacios, A., Charbonnel, C., Talon, S., & Siess, L. 2006, A&A, 453, 261
Parker, E. N. 1993, ApJ, 408, 707
Pedlosky, J. 1987, Geophysical Fluid Dynamics (New York: Springer)
Pinsonneault, M. 1997, ARA&A, 35, 557
Pizzolato, N., Maggio, A., Micela, G., Sciortino, S., & Ventura, P. 2003, A&A, 397, 147
Rempel, M. 2004, ApJ, 607, 1046
Rempel, M. 2005, ApJ, 622, 1320

Rogers, T. 2011, ApJ, 733, 12
Rogers, T., & Glatzmaier, G. 2005, MNRAS, 364, 1135
Rogers, T., & Glatzmaier, G. 2006, ApJ, 653, 756
Rogers, T., Glatzmaier, G., & Jones, C. A. 2006, ApJ, 653, 765
Rüdiger, G., & Kitchatinov, L. 1997, Astron. Nachr., 318, 273
Rüdiger, G., & Kitchatinov, L. 2007, New J. Phys., 9, 302
Saar, S. H., & Brandenburg, A. 1999, ApJ, 524, 295
Schatzman, E. 1962, Ann. Astron., 25, 18
Schou, J., Antia, H. M., Basu, S., et al. 1998, ApJ, 505, 390
Skumanich, A. 1972, ApJ, 171, 565
Soward, A. 2007, in Mathematical Aspects of Natural Dynamos, ed. E. Dormy & A. Soward (London: CRC Press), 151
Spada, F., Lanzafame, A. C., & Lanza, A. F. 2010, MNRAS, 404, 641
Spiegel, E. A., & Zahn, J.-P. 1992, A&A, 265, 106
Spruit, H. C. 1999, A&A, 349, 189
Strugarek, A., Brun, A. S., & Zahn, J.-P. 2011, A&A, 532, 34
Tayler, R. J. 1973, MNRAS, 161, 365
Thompson, M. J., Christensen-Dalsgaard, J., Miesch, M. S., & Toomre, J. 2003, ARA&A, 41, 599
Tobias, S. M., Brummell, N. H., Clune, T. L., & Toomre, J. 2001, ApJ, 549, 1183
von Rekowski, B., & Rudiger, G. 1998, A&A, 335, 679
Weber, E. J., & Davis, L. 1967, ApJ, 148, 217
Wood, T. S., & McIntyre, M. E. 2011, J. Fluid Mech., 677, 445
Zahn, J.-P. 1991, A&A, 265, 115
Zahn, J.-P. 1992, A&A, 252, 179
Zahn, J.-P., Talon, S., & Matias, J. 1997, A&A, 322, 320